Improving Fatigue Strength of Polymer Concrete using Nanomaterials with Field Implementation

MAHMOUD REDA TAHA, Ph.D.
RAFI TAREFDER, Ph.D.

SPTC14.1-66-F
SPTC15.1-49-F

Southern Plains Transportation Center
201 Stephenson Parkway, Suite 4200
The University of Oklahoma
Norman, Oklahoma 73019

DISCLAIMER

The contents of this report reflect the views of the authors, who are responsible for the facts and accuracy of the information presented herein. This document is disseminated under the sponsorship of the Department of Transportation University Transportation Centers Program, in the interest of information exchange. The U.S. Government assumes no liability for the contents or use thereof.

Technical Report Documentation Sheet

1. REPORT NO.	2. GOVERNMENT ACCESSION NO.	3. RECIPIENTS CATALOG NO.
SPTC 14.1-66/SPTC15.1-49		

4. TITLE AND SUBTITLE	5. REPORT DATE
Improving fatigue strength of polymer concrete using nanomaterials with field implementation	October 16, 2018
	6. PERFORMING ORGANIZATION CODE
7. AUTHOR(S)	8. PERFORMING ORGANIZATION REPORT
Mahmoud Reda Taha and Rafi Tarefder	University of New Mexico
9. PERFORMING ORGANIZATION NAME AND ADDRESS	10. WORK UNIT NO.
School of Civil Engineering University of New Mexico 210 University Blvd NE MSC01 1070, room 3020 Albuquerque, NM 87131-0001	11. CONTRACT OR GRANT NO. **DTRT13-G-UTC36**
12. SPONSORING AGENCY NAME AND ADDRESS	13. TYPE OF REPORT AND PERIOD COVERED
Southern Plains Transportation Center 201 Stephenson Pkwy, Suite 4200 The University of Oklahoma Norman, OK 73019	Final April 2015 – October 2018
	14. SPONSORING AGENCY CODE

15. SUPPLEMENTARY NOTES

Matching fund provided by New Mexico Department of Transportation (NMDOT) and Industrial Partners (Transpo Industries and Epoxy Chemicals Inc.)

16. ABSTRACT

Polymer concrete (PC) is that type of concrete where the cement binder is replaced with polymer. PC is often used to improve friction and protect structural substrates in reinforced concrete and orthotropic steel bridges. However, its low fatigue performance, limited fracture toughness and tendency to debond pose expensive maintenance challenges for highway bridges. This research investigated the use of nanomaterials such as multi-walled carbon nanotubes (MWCNTs) and alumina nanoparticles (ANPs) to produce PC with superior bond strength, fracture toughness and fatigue strength. A total of 20 different PC mixes were containing up to 3.0 wt.% content of nanomaterial were developed and examined. Mechanical characterization methods including compressive, flexural, bond and tensile strengths, ductility (strain at failure), toughness, fracture toughness and fatigue were conducted. Finite element modeling was also utilized to understand the shear stresses in PC-steel interface. Microstructural analysis revealed the chemical effects of incorporating nanomaterials in PC. The results show improvements in all mechanical performances of PC reaching 170% in fracture toughness, 1200% in fatigue life, 135% in ductility with a decrease in tensile and compressive strengths by about 15%. Furthermore, experimental work showed the ability to use pristine MWCNTs to self-monitor PC under static and cyclic loads. Finally, field implementation of PC with nanomaterials showed the ability to perform self-monitoring of PC under standard traffic loading. Field implementation is included.

17. KEY WORDS	18. DISTRIBUTION STATEMENT
Nanomaterials, polymer concrete, fatigue	No restrictions. This publication is available at www.sptc.org and from the NTIS.

19. SECURITY CLASSIF. (OF THIS REPORT)	20. SECURITY CLASSIF. (OF THIS PAGE)	21. NO. OF PAGES	22. PRICE
Unclassified	Unclassified	71 + cover	

SI* (MODERN METRIC) CONVERSION FACTORS

APPROXIMATE CONVERSIONS TO SI UNITS

SYMBOL	WHEN YOU KNOW	MULTIPLY BY	TO FIND	SYMBOL
		LENGTH		
in	inches	25.4	millimeters	mm
ft	feet	0.305	meters	m
yd	yards	0.914	meters	m
mi	miles	1.61	kilometers	km
		AREA		
in^2	square inches	645.2	square millimeters	mm^2
ft^2	square feet	0.093	square meters	m^2
yd^2	square yard	0.836	square meters	m^2
ac	acres	0.405	hectares	ha
mi^2	square miles	2.59	square kilometers	km^2
		VOLUME		
fl oz	fluid ounces	29.57	milliliters	mL
gal	gallons	3.785	liters	L
ft^3	cubic feet	0.028	cubic meters	m^3
yd^3	cubic yards	0.765	cubic meters	m^3
	NOTE: volumes greater than 1000 L shall be shown in m^3			
		MASS		
oz	ounces	28.35	grams	g
lb	pounds	0.454	kilograms	kg
T	short tons (2000 lb)	0.907	megagrams (or "metric ton")	Mg (or "t")
		TEMPERATURE (exact degrees)		
^oF	Fahrenheit	5 (F-32)/9 or (F-32)/1.8	Celsius	^oC
		ILLUMINATION		
fc	foot-candles	10.76	lux	lx
fl	foot-Lamberts	3.426	candela/m^2	cd/m^2
		FORCE and PRESSURE or STRESS		
lbf	poundforce	4.45	newtons	N
lbf/in^2	poundforce per square inch	6.89	kilopascals	kPa

*SI is the symbol for the International System of Units. Appropriate rounding should be made to comply with Section 4 of ASTM E380. (Revised March 2003)

APPROXIMATE CONVERSIONS FROM SI UNITS				
SYMBOL	**WHEN YOU KNOW**	**MULTIPLY BY**	**TO FIND**	**SYMBOL**
		LENGTH		
mm	millimeters	0.039	inches	in
m	meters	3.28	feet	ft
m	meters	1.09	yards	yd
km	kilometers	0.621	miles	mi
		AREA		
mm^2	square millimeters	0.0016	square inches	in^2
m^2	square meters	10.764	square feet	ft^2
m^2	square meters	1.195	square yards	yd^2
ha	hectares	2.47	acres	ac
km^2	square kilometers	0.386	square miles	mi^2
		VOLUME		
mL	milliliters	0.034	fluid ounces	fl oz
L	liters	0.264	gallons	gal
m^3	cubic meters	35.314	cubic feet	ft^3
m^3	cubic meters	1.307	cubic yards	yd^3
		MASS		
g	grams	0.035	ounces	oz
kg	kilograms	2.202	pounds	lb
Mg (or "t")	megagrams (or "metric ton")	1.103	short tons (2000 lb)	T
		TEMPERATURE (exact degrees)		
^oC	Celsius	1.8C+32	Fahrenheit	^oF
		ILLUMINATION		
lx	lux	0.0929	foot-candles	fc
cd/m^2	$candela/m^2$	0.2919	foot-Lamberts	fl
		FORCE and PRESSURE or STRESS		
N	newtons	0.225	poundforce	lbf
kPa	kilopascals	0.145	poundforce per square inch	lbf/in^2

*SI is the symbol for the International System of Units. Appropriate rounding should be made to comply with Section 4 of ASTM E380. (Revised March 2003)

IMPROVING FATIGUE STRENGTH OF POLYMER CONCRETE USING NANOMATERIALS AND FIELD IMPLEMENTATION

Final Report

October 2018

Mahmoud Reda Taha, PhD

Rafi Tarefder, PhD

University of New Mexico

Southern Plains Transportation Center

201 Stephenson Pkwy, Suite 4200

The University of Oklahoma

Norman, Oklahoma 73109

Contents

LIST OF FIGURES

LIST OF TABLES

EXECUTIVE SUMMARY

Polymer concrete (PC) overlays are typically used to improve friction in highway bridges and parking structures and to protect the structural substrate in steel and concrete bridges. Limited bond strength and fatigue failures of PC overlays have been observed and pose an expensive maintenance challenges for highway bridges. In spite of its superior durability performance, compared with normal concrete overlays, PC overlays fracture toughness is slightly higher than normal concrete and thus has limited crack propagation resistance. Such criteria limit PC's ability to resist debonding or fatigue damage. During the last two decades, significant improvements to polymer materials were made by considering nanomaterials. Research efforts proved the ability of nanomaterials to alter polymers and to produce new polymer nanocomposite materials with improved strength, stiffness and resistance to degradation. Examples of improvement of polymers and polymer composites using carbon nanotubes, nanosilica and nanoclay have been reported in the literature.

This study proposes improving the bond strength, ductility, fracture toughness and fatigue life of PC overlays using nanomaterials such as multi-walled carbon nanotubes (MWCNTs) or alumina nanoparticles (ANPs). Different contents of each nanoparticle were investigated to define the optimal content desired for improved mechanical performance. In particular, two types of MWCNTs namely pristine (P-MWCNTs) and carboxyl functionalized MWCNTs (COOH-MWCNTs) were investigated. P-MWCNTs also resulted in improved electrical conductivity of PC enabling structural health monitoring (SHM) by correlating mechanical damage to changes in electrical conductivity or electrical resistance. Mechanical characterization methods included tensile, compressive and flexural strength tests to evaluate ductility (strain at failure), fatigue, toughness and fracture toughness. Further analysis of the bond strength of PC-steel surfaces was investigated using slant shear method and finite element analysis (FEA) using ABAQUS. Microstructural analysis utilizing scanning electron microscope (SEM) and Fourier transform infrared spectroscope (FTIR) were used to examine proper dispersion and investigate potential chemical reaction between the polymer and the nanomaterials. Special fatigue, tension and fracture toughness test apparatuses were developed and used to evaluate performance of PC with nanomaterials.

SEM images of all epoxy nanocomposite reveal that uniform dispersion was achieved using shear mixing and ultrasonication. Thus, this method of dispersion was kept constant for all PC mixes. The experimental results show that PC provide superior ductility over conventional concrete materials. PC exhibit large tensile strengths up to 11.5 MPa and tensile strain at failure of 1.8%. Incorporating P-MWCNTs resulted in small decrease in tensile strength with a minimum appreciable tensile strength of 9 MPa. The strain at failure, however, increased to 3.2%. COOH-MWCNTs results show a different behavior by increasing the tensile strength up to a maximum of 15.4 MPa with a decrease in strain at failure to 0.8%. ANPs showed similar results to that of P-MWCNTs with a minimum of 9.5 MPa and an improved tensile strain at failure of 4.9%.

Thus, incorporating nanoparticles resulted in a maximum decrease of tensile strength by 22% countered by a maximum improvement in strain at failure by 91%. The significant improvements achieved were clearly reflected with improvements in PC's toughness by a maximum of 80%, and 135% for P-MWCNTs and ANPs respectively.

P-MWCNTs were solely investigated for fatigue performance as COOH-MWCNTs bond with the host polymer matrix and ANPs do not provide a conductive network. Fatigue performance of P-MWCNTs PC mixes showed improvements in fatigue life up to 1240% at 2.0 wt.% content. Furthermore, the percolation level is achieved at such low content allowing mechanical damage to be correlated to the change in electrical resistance of PC. Thus, self-sensing of PC is possible enabling the observation of damage propagation in PC overlays using electrical measurements. PC samples in all mechanical tests exhibited non-linear behavior redeeming linear elastic fracture mechanics (LEFM) analysis, often used for concrete, invalid. Quasi-brittle fracture mechanics (QBFM) was therefore used for the analysis of the fracture toughness parameters of PC with nanoparticles. Total fracture energy parameter combining both elastic and J-integral values of fracture toughness was used to describe the fracture toughness of PC. Results show that incorporating P-MWCNTs, COOH-MWCNTs and ANPs improve the total fracture toughness by 52%, 112%, and 128% respectively. Improvements with P-MWCNTs mixes were achieved mainly with plastic fracture toughness while ANPs and COOH-MWCNTs achieved improvements in both elastic and plastic fracture toughness.

FEA was utilized to examine the true shear stresses inflicted to PC-steel bond. Analysis revealed the true shear stresses are formed at locations of maximum stiffness mismatch. At these locations, minimum thickness of PC to steel is present and the shear stresses are increased by up to 100%. Nonetheless, PC with nanoparticles provided strong bond to steel substrates with improvement in bond strength up to 51%. Finally, FTIR spectrographs reveal that both P-MWCNTs and ANPs delay the epoxy polymerization and thus reduce PC crosslinking density thus improve ductility. On the other hand, COOH-MWCNTs react with the host epoxy matrix forming C=O ester bonds that increase the level of crosslinking density and improve strength.

PC incorporating nanoparticles provide a promising material that can be engineered to provide mechanical enhancements in bond strength, ductility, fatigue life and fracture toughness. Those parameters not only reduce the required maintenance associated with PC overlays but also provide a promising material alternative to conventional concrete in structural applications. Finally, field implementation of PC with nanomaterials was performed. Field trials at a location used for parking at University of New Mexico (UNM) campus was implemented. Field implementation showed the ability to perform self-monitoring of PC under standard traffic loading. With the continuous decrease in cost of nanomaterials and the low content required to produce PC with nanomaterials, we anticipate PC with nanomaterials to be available for industrial applications and use in the field in the very near future.

INTRODUCTION

Polymer concrete (PC) is a composite material in which a polymer matrix such as epoxy, unsaturated polyester (UP) or Poly methyl methacrylate (PMMA) replaces Portland cement as a binder to bond aggregate together [1]. PC is used in numerous applications including bridge deck overlays, machine foundations, pipes and pipe liners, hazard materials storage and architectural panels [1-2]. PC gained worldwide attention in the construction field since the 1970s because of its superior durability and attractive mechanical properties. Typical mechanical properties of PC incorporate a compressive strength of 100-120 MPa, a tensile strength of 8-10 MPa, a flexural strength of 20-24 MPa and a wide range of modulus of elasticity in the range of 20-40 GPa depending on the type of resin and aggregates used [3-4]. Hsu and Fowler [5] showed that PC has superior fatigue strength compared with conventional Portland cement concrete. PC has also been reported to have excellent bond strength to different substrates including concrete and steel [6]. The improved mechanical characteristics of PC stem from a tight microstructure which allows PC to have excellent durability as well [7]. The above attractive mechanical and durability characteristics promoted the use of PC as overlays in bridge decks and parking structures. While PC overlays have been used in numerous bridges and parking structures worldwide, they have been reported to suffer fatigue cracks that lead to premature debonding [1]. Methods to improve fatigue strength of PC have been sought [8].

Nanoparticles such as nanoclay, alumina nanoparticles, carbon nanotubes, and carbon nanofibers have been recently examined to improve polymer materials. Jo et al. [9] reported improved mechanical and thermal performance of unsaturated polyester (UP) concrete mixed with montmorillonite (MMT). Moreover, modified nanoclay was added to epoxy concrete and improved some mechanical properties, but it decreased tensile and flexural strengths [10]. Alumina nanoparticles (ANPs) were successively used with cementitious materials to improve strength development of calcium silicate hydrate (CSH) gels and to limit the interfacial transition zone (ITZ) between paste and aggregate and improve its characteristics [11-13]. Furthermore, the mechanical properties including tensile strength and strain of latex modified concrete were reported to be significantly improved at low CNTs' content [14]. CNTs are tabular structure made from concentrically rolled single or multiple graphite sheets. CNTs were first introduced as single-walled carbon nanotubes (SWCNTs) and proved to have superior mechanical properties compared to many other nanomaterials, but they were typically expensive. High-purity SWCNTs were synthesized and grown using thermal Chemical vapor deposition (CVD) at a growth temperature of and above 700 ^{o}C [15].

Multi-walled carbon nanotubes (MWCNTs) appeared later as a cheaper alternative form of CNTs. Using the CVD method, MWCNTs are synthesized at a relatively low temperature of 450 ^{o}C compared to 700 ^{o}C for SWCNTs [16]. In order to generate a

chemical bond between CNTs and polymer matrix, CNTs need to be functionalized by chemical groups that can react with the polymer matrix. Functionalization is a process of surface treatment where a chemically attractive functional group is planted on the surface of the nanomaterial. Functionalized nanomaterials proved necessary for good dispersion inside polymer matrices [17-18]. Furthermore, surface functionalization enables nanomaterials to cross the length scale by generating a chemical bond with the polymer matrix and thus altering the original polymer and generating a new polymer nanocomposite [19] and by participating as reinforcement (fibers or platelets) that hinders chain movement and bridge microcracks to improve mechanical and fracture properties of the polymer nanocomposite [20]. Swain et al. [21] reported using saline functionalized MWCNTs in producing polymer nanocomposites with improved mechanical properties. Soliman et al. [22] showed the significance of carboxylic group functionalization on improving the off-axis tensile strength of woven carbon fiber composites. Furthermore, wax coated MWCNTs enhanced the electrical conductivity and improved the mechanical properties of high-density polyethylene system [23].

Alumina nanoparticles (ANPs) provide a different approach to altering the mechanical properties of polymers and other materials. While MWCNTs are classified as two dimensional nanoparticles, ANPs are three dimensional nanoparticles with significantly higher surface area allowing high chemical reactivity [24]. Li et al. [11] examined the elastic modulus and compressive strength of cement concrete including ANPs at 3, 7 and 28 days of curing and reported 143% increase in mortar elastic modulus using 5% ANPs after the 28 days curing period. However, no increase in compressive strength was reported [11]. In order to obtain eco-efficient cements, Campillo et al. [12] used agglomerated dry alumina and colloidal alumina in hydrated belite cements. The addition of two types of ANPs increased the 7-day compressive strength of the mixes. Hosseini et al. [13] investigated the effect of different kinds of nano-particles including SiO_2, Al_2O_3, clay and $CaCO_3$ on performance of cementitious materials. As a result, they pointed out that with the addition of nano-particles flexural strength of the mixes was improved [13]. To improve polymers, Dorigato and Pegoretti [25] used ANPs dispersed in epoxy to investigate thermo-mechanical behavior of the ANPs- epoxy mixture. It was shown that ANPs could effectively improve the stiffness, adhesion strength, and fracture toughness of epoxy [25]. Furthermore, Zabihi et al. [26] synthesized epoxy nanocomposites with various weight content of ANPs and showed that inclusion of ANPs significantly affects the thermal degradation kinetics of the epoxy nanocomposites [26].

In the last two decades, additives have been added to the PC binder system or replaced some of the aggregate to enhance one or more of the mechanical or chemical properties. These additives included polymeric wastes such as recycled plastic bottles [27], recycled PC [28], rubbers and electrical cable wastes [29]. Prior work also included replacing aggregate filler in PC by fly ash [30]. Moreover, nanoscale inorganic particles such as nanoclay, carbon nanotubes, and carbon nanofibers were added to polymer matrices to manufacture polymer nanocomposites. With homogeneous dispersion of the

nanoscale particles in polymer matrices, polymer nanocomposites experience improved properties compared with pure polymer matrices [31-32]. New generation of latex modified concrete with enhanced properties was also produced by incorporating Carbon Nano-Tubes (CNTs) in the polymer matrix during PC fabrication [33]. Here we suggest altering polymer concrete using multi-wall carbon nanotubes.

Many researchers have studied the effects of carbon nanotubes on tensile properties of hardened epoxy samples through various sample dimensions and various mechanical tests namely; direct tension, flexural and through dynamic modulus analyser (DMA) tests [34-42]. The content introduced often ranged between 0.1 and 2.0 wt.% content [34-36, 39-43] with few divergent up to 5.0 and 10.0 wt.% [38, 44] and as low as 0.01 wt.% [37]. The inclusion of MWCNTs reported improvements in tensile strength in the range of 9 to 51% of epoxy and PMMA composites [34-43]. An increase of tensile strength was observed with the increase of content but in a decaying fashion. Wang et al. showed that parallel aligned single walled CNTs improve the tensile strength as CNTs contents increase up to 168% [44]. Alignment in the perpendicular direction however showed smaller improvements and further a decrease in strength beyond 2.0 wt.% content [44]. The variation in the reported results therefore is attributed to the random orientation of CNTs resulting in non-uniform strengthening mechanisms as well as the different chemical interaction between epoxy and MWCNTs.

Literature on fracture toughness of epoxy polymer systems is often incomplete and is most often limited to the critical stress intensity factor (KIc) [45-51]. For instance, while the vast majority of literature show an increase in fracture toughness [45-57] and further improvements with the increase in content [45-47, 58], Ma et al. and Opelt et al. showed a decrease of KIc with the increase in content of pristine MWCNTs [58, 59]. The inclusion of significantly stiffer materials to a polymer matrix (1 TPa compared to ~1-10 GPa) along with the change in chemical bonds and crosslinking density alters the material's stiffness and strength. For example, the elastic modulus has been shown to increase due to the incorporation of MWCNTs by 3 – 26% [48, 50, 53-56, 59-60]. Therefore, reports on the critical energy release rate (GIc) or the critical J-integral (JIc) provide more thorough fracture toughness representation. In fact, researchers found greater increase in fracture toughness in the range of 56 – 138% measured by GIc compared to 27-51% measured by KIc [52-55, 57-58]. The content of nanotubes examined to induce improvements in fracture toughness often ranged between 0.05 and 1.5 wt.% content [45-46, 48-50, 52-53, 56-57, 59]. Yu et al. and Ma et al. examined higher contents up to 3.0 and 5.0 wt.% respectively [47, 59]. The polymer-nanotubes chemical interaction occurs differently based on the content of nanotubes and the type of polymer used. This is reflected for example at 1.0 wt.% content of pristine MWCNTs where White and Sue showed a 42% increase in KIc compared to 27% by Tang et al. On the other hand, Zhou et al. showed similar improvements to Tang et al. of 30% at much lower content (0.3 wt.%) while Yu et al. reported parallel 33% improvements however at much higher content (3.0 wt.%) [47-48, 54]. The nano-induced chemical effects alter polymers chemically modifying the material's stress transfer mechanism.

This is apparent as MWCNTs epoxy samples show a change in the glass transition temperature (Tg) as it was reported to increase [46, 54-55, 58] or a decrease [53, 56]. On the other hand, MWCNTs provide significantly high aspect ratio that lead to microfiber-like crack arresting mechanisms such as fiber pull-out or bridging [53]. As a result, analysis of the effects of MWCNTs of fracture toughness are only valid when establishing both mechanical and chemical features. Only then the crack energy consumption mechanisms can be identified and the change of fracture behavior caused by nanotubes is identified.

EXPERIMENTAL METHODS

Materials

1. Polymers

The polymer used is polysulfide epoxy including silane. This epoxy is usually used as an overlay material for repair of bridge decks. The epoxy consists of two components, epoxy resin and epoxy hardener. The resin is mixture of Bisphenol A/Epichlorohydrin Epoxy Resin including silane. The hardener is Diethylenetriamine (DETA), Phenol, 4,4'-(1-methylethylidene)bis-, and Tetraethyllenepentamine.

2. Filler

In all mixes crystalline silica (quartz) and ceramic microspheres powder was used as mixing filler to produce the slurry to be cast and harden.

3. Nanomaterials

Pristine and functionalized with carboxyl group MWCNTs namely P-MWCNTs and COOH-MWCNTs respectively were provided by Cheap Tubes, Inc. Both have an outer dimension of 20-30 nm, an inner dimension of 5-10 nm, and a length of 10-30 μm. The Alumina nanoparticles (ANP) used is Alumina Oxide (Al_2O_3) Nano-particles of 50 nm maximum particle size provided by Sigma Aldrich Inc.

Procedure for synthesis and mixing of polymer nanocomposite

For the neat polymer, the required amount of resin and hardener were mixed together for 2-3 minutes using a low speed mixer, after which the required aggregate filler was added. Mixing continued for 2-3 minutes until the mixture was uniform. For the nanocomposite mix, the nanoparticles (e.g. MWCNTs) were added to the required amount of the resin, the mix was stirred for 2 hours at 110 ^{o}C using magnetic stirring. This relatively high mixing temperature was used to reduce the resin viscosity and improve the dispersion of nanomaterials. The mix was then sonicated for 2 additional hours at 60 ^{o}C. During the sonication, sound waves are generated from the transducer and radiate through the liquid causing high and low pressures. At the low pressure

stage, millions of microscopic bubbles are formed; during the high pressure stage, the previous bubbles collapse releasing high amount of energy and improving the dispersion of the nanoparticles. **Fig. 1** shows the mixing process for the polymer nanocomposite. The polymer resin nanocomposite was left to reach room temperature and then mixed with the hardener for 2-3 minutes. The required aggregate was then added and mixing continued for 2-3 additional minutes until the mixture looked uniform. **Table 1** provides the neat (control) mix and PC mixes incorporating nanomaterials as percentage of the epoxy resin by weight.

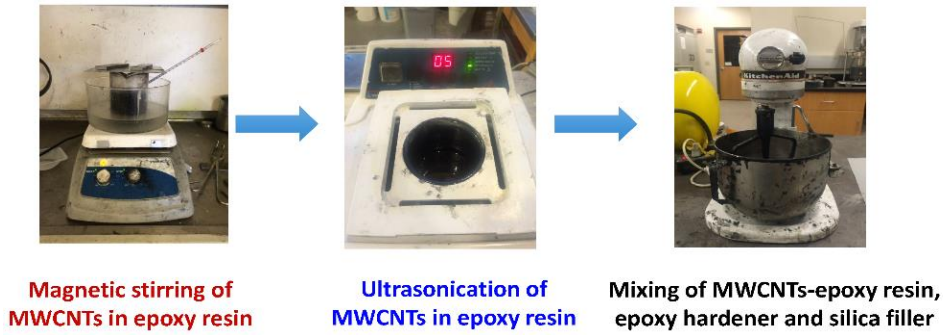

Figure 1: Technique for mixing PC incorporating MWCNTs: Magnetic stirring of MWCNTs in the epoxy resin (first dispersion step). The ultrasonication of that resin (the second and last dispersion step). Mixing the resin incorporating MWCNTs with the hardener and aggregate to produce PC

Table 1: Mix proportions for polysulfide siloxane epoxy nanocomposites kg/m3 (lb/ft^3).

Mix designation	Resin	Hardener	Filler	Nanomaterials	Nano content
PC-Neat	288 (18)	128 (8)	1570 (98)	None	0.00 (0.00)
PCNP-0.1	288 (18)	128 (8)	1570 (98)	P-MWCNTs	0.29 (0.018)
PCNP-0.25	288 (18)	128 (8)	1570 (98)	P-MWCNTs	0.72 (0.045)
PCNP-0.5	288 (18)	128 (8)	1570 (98)	P-MWCNTs	1.44 (0.09)
PCNP-0.75	288 (18)	128 (8)	1570 (98)	P-MWCNTs	2.16 (0.135)
PCNP-1.0	288 (18)	128 (8)	1570 (98)	P-MWCNTs	2.88 (0.18)
PCNP-1.5	288 (18)	128 (8)	1570 (98)	P-MWCNTs	4.32 (0.27)
PCNP-2.0	288 (18)	128 (8)	1570 (98)	P-MWCNTs	5.76 (0.36)
PCNP-3.0	288 (18)	128 (8)	1570 (98)	P-MWCNTs	8.64 (0.54)
PCNC-0.5	288 (18)	128 (8)	1570 (98)	COOH-MWCNTs	1.44 (0.09)
PCNC-1.0	288 (18)	128 (8)	1570 (98)	COOH-MWCNTs	2.88 (0.18)
PCNC-1.5	288 (18)	128 (8)	1570 (98)	COOH-MWCNTs	4.32 (0.27)
PCNC-2.0	288 (18)	128 (8)	1570 (98)	COOH-MWCNTs	5.76 (0.36)
PCNA-0.5	288 (18)	128 (8)	1570 (98)	ANPs	1.44 (0.09)
PCNA-1.0	288 (18)	128 (8)	1570 (98)	ANPs	2.88 (0.18)
PCNA-2.0	288 (18)	128 (8)	1570 (98)	ANP	5.76 (0.36)
PCNA-3.0	288 (18)	128 (8)	1570 (98)	ANP	8.64 (0.54)
PC-Neat-90F	288 (18)	128 (8)	1410 (88)	None	0.00 (0.00)
PCNP-2.0-90F	288 (18)	128 (8)	1410 (88)	P-MWCNTs	5.76 (0.36)
PCNA-2.0-90F	288 (18)	128 (8)	1410 (88)	ANP	5.76 (0.36)

ANALYSIS

Flexural Testing

Three-point bending test under static loads were performed to investigate the behavior of the PC overlay using a MTS Bionex servo hydraulic machine. Static loading 3-point bending was conducted on 25 x 25 x 150 mm specimen as displacement control test with a loading rate in the range of 0.20-0.45 mm/min. Throughout the test, time, load, and displacement were recorded using MTS® 793 data acquisition system with a sampling rate of 1 Hz. Five specimens of each PC mix were tested under flexural load until failure. The results show that incorporating MWCNTs in the PC can increase the flexural load capacity of PC at certain percentages. Mixes incorporating COOH-MWCNTs provided an overall improvement in modulus of rupture (MOR) while P-

MWCNTs and ANPs averaged lower MOR. **Figures 2, 3 and 4** show the results of MOR for all mixes. The improvements in MOR ranged from 21% to 42% for COOH-MWCNTs, 1% to 9% for P-MWCNTs and 0 to 30% for ANP. The drop on the other hand was insignificant with -13% to -19% for P-MWCNTs, -14% for COOH-MWCNTs, -4% to -17% for ANP. Nonetheless, all mixes incorporating showed significant increase in ductility as the maximum deflection increased as reflected as well in direct tension test discussed later.

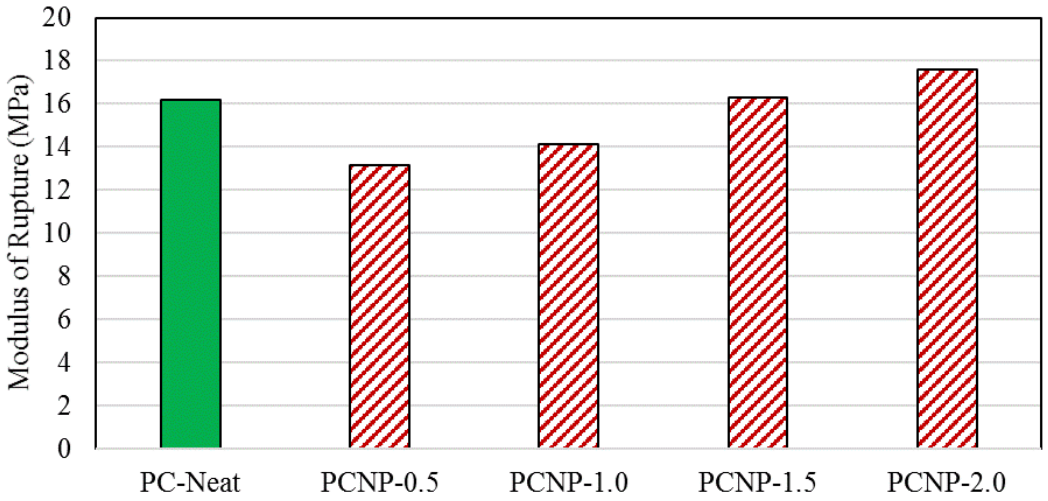

Figure 2: Flexural strength of PC with and without P-MWCNTs showing change from -19% to 9% from PC-Neat.

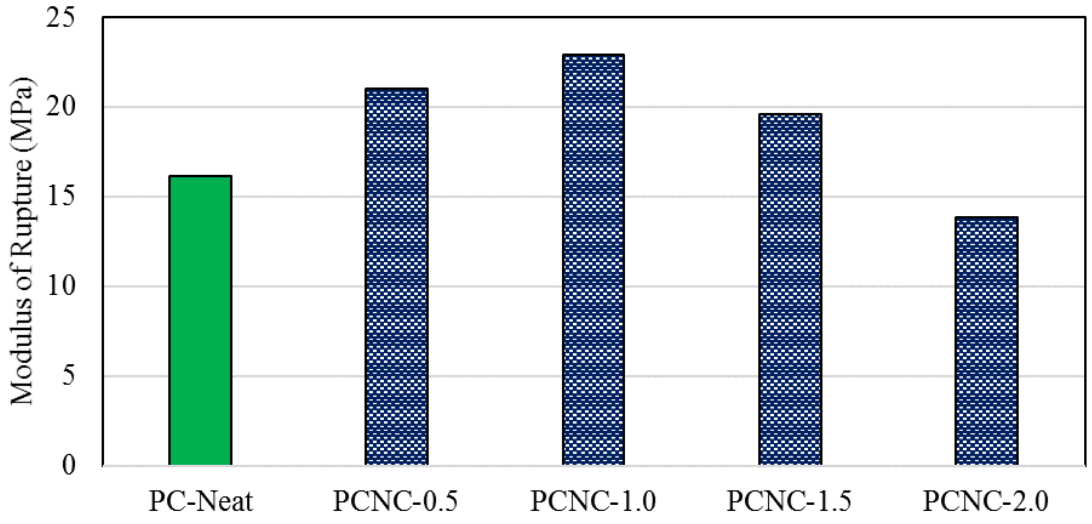

Figure 3: Flexural strength of PC with and without COOH-MWCNTs showing change from -14% to 42% from PC-Neat.

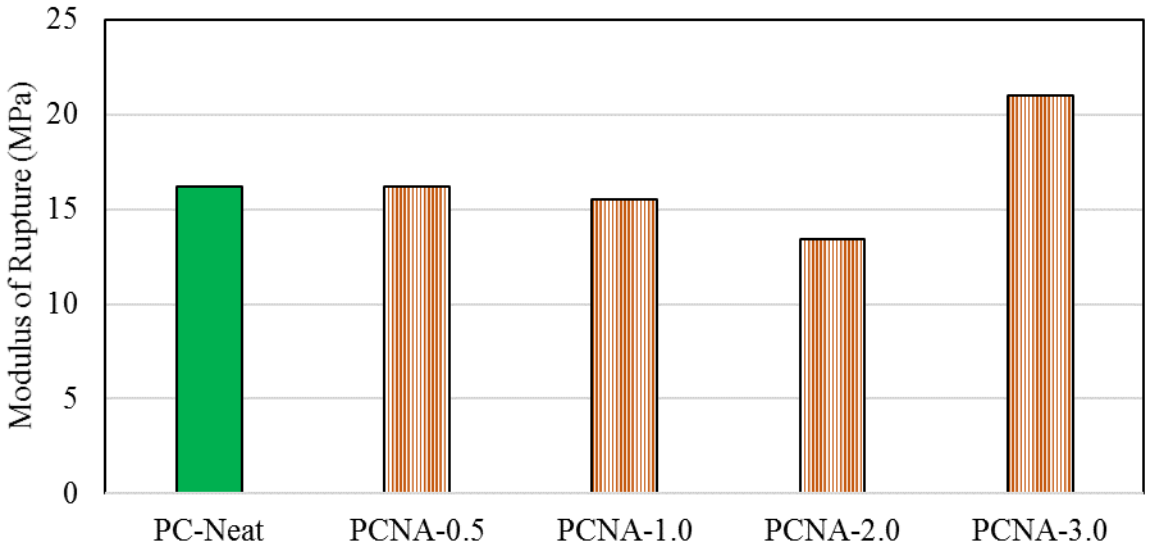

Figure 4: Flexural strength of PC with and without ANPs showing change from -17% to 30% from PC-Neat.

Tension Testing

The tensile strength of nanocomposite PC (NCPC) was evaluated using direct tension test on standard dumbbell-shaped samples. The test was performed using a MTS Bionex servo hydraulic machine. The test was performed according to ASTM D638-14. In order to produce NCPC type III samples, specific molds were designed to cast samples ready for testing. **Figure 5** shows both type III dimensions and their specific molds. NCPC samples were treated as rigid samples with a loading rate of 3.75 mm/min. Strain recording extensometer was used to measure tensile strain at the mid-section of samples were maximum strain is often observed. In order to produce NCPC with high strain and strength, samples were heat cured at 60℃. Also, samples containing reduced filler at 90% of the original mix were tested. Five samples per mix were used and the average of all is shown in **Figures 6, 7, 8, 9,10 and 11** for tensile strength, maximum strain, maximum displacement, stress-strain curves and toughness respectively.

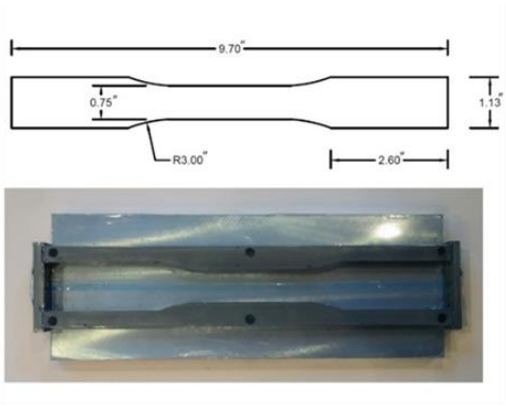

(a) Tension sample type III dimensions as produced by the specific molds shown

(b) PC tension samples produced

(c) PC sample in testing using extensometer

Figure 5: Tension sample molds, dimensions and sample.

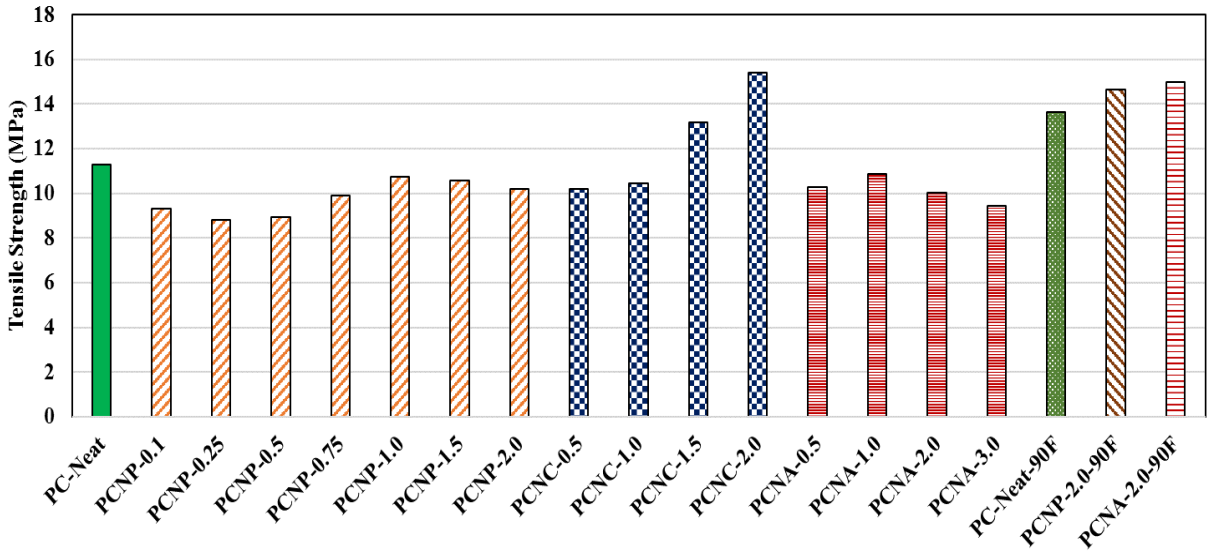

Figure 6: Tensile strength of PC mixes using different nanomaterials as well as 90% filler content.

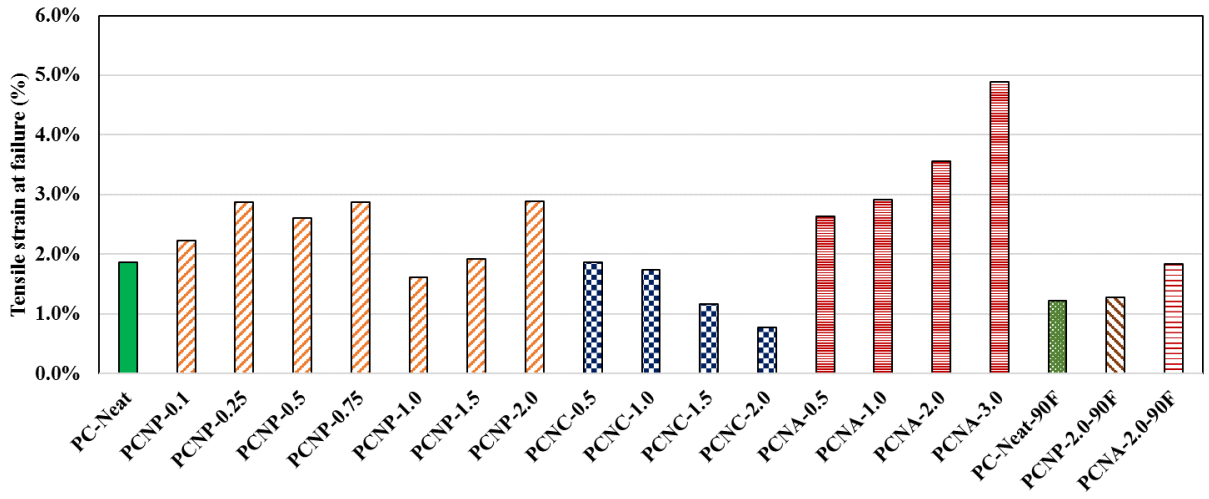

Figure 7: Tensile strain at failure of PC mixes using different nanomaterials as well as 90% filler content.

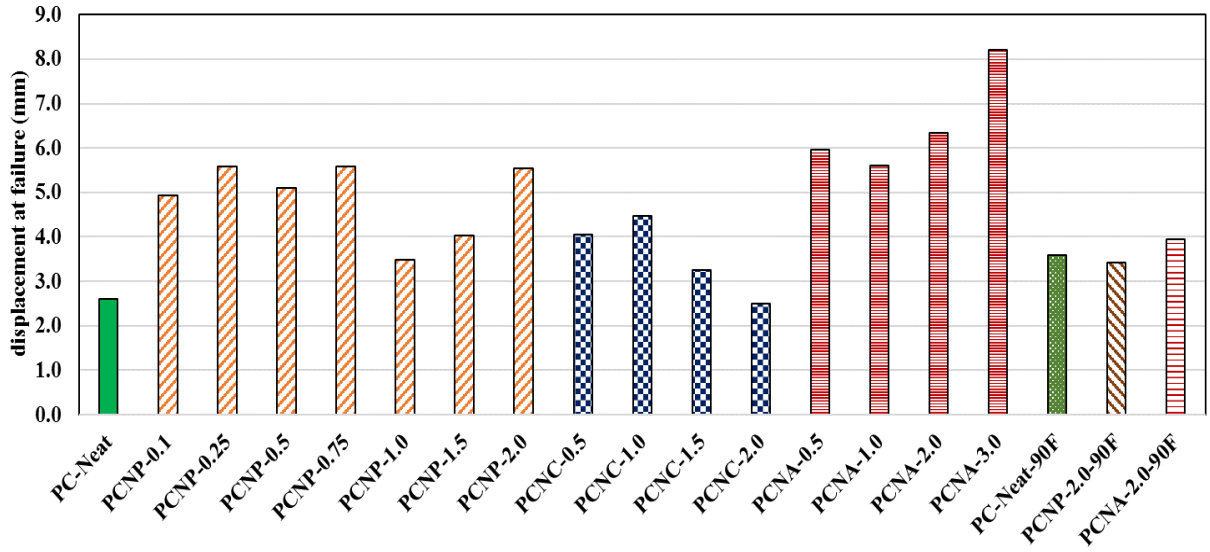

Figure 8: Tensile displacement at failure of PC mixes using different nanomaterials as well as 90% filler content.

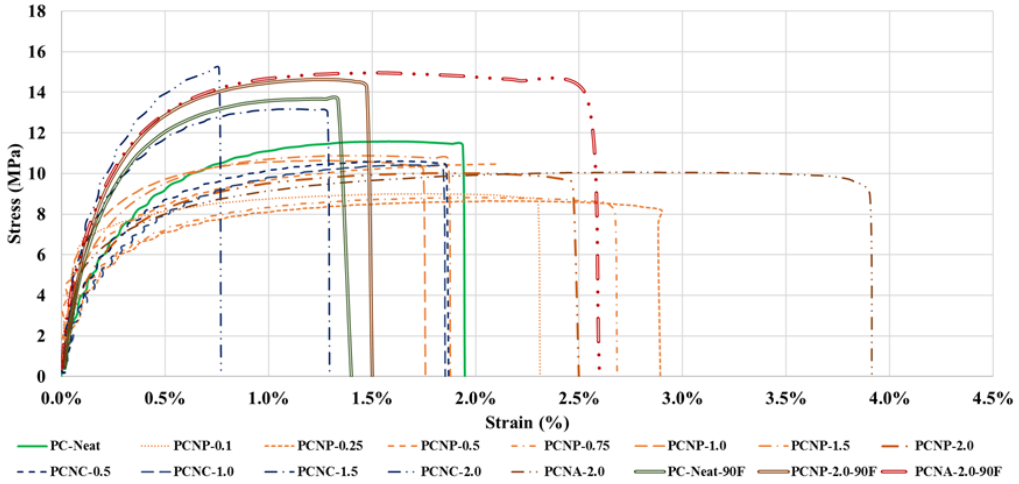

(a) All NCPC mixes heat cured at 60℃ stress-strain diagrams for tensile test.

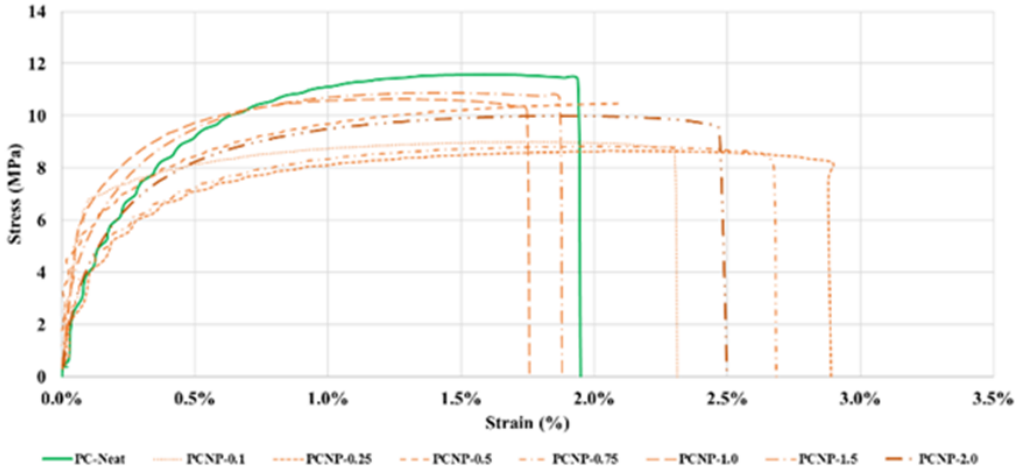

(b) NCPC incorporating P-MWCNTs stress-strain curves for tensile test

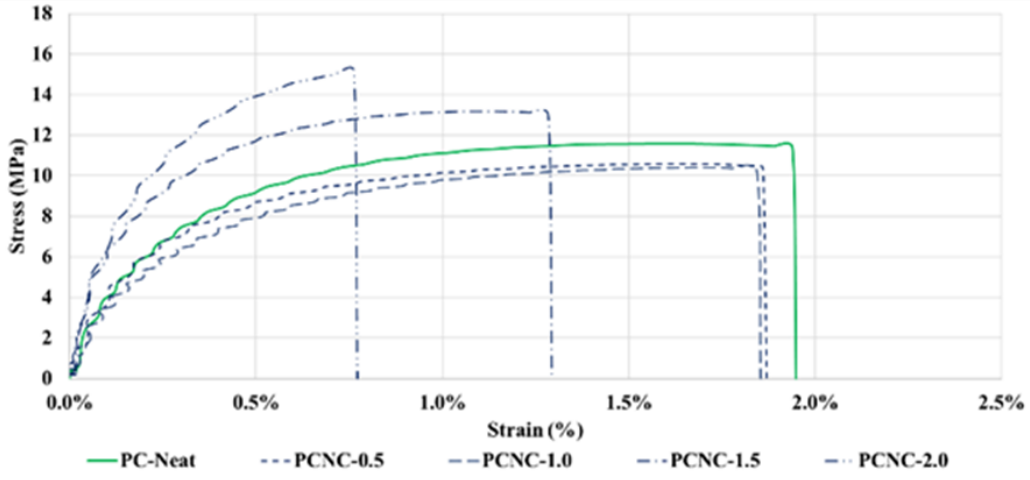

(c) NCPC incorporating COOH-MWCNTs stress-strain curves for tensile test.

Figure 9: Stress-strain diagrams for NCPC mixes in tensile test.

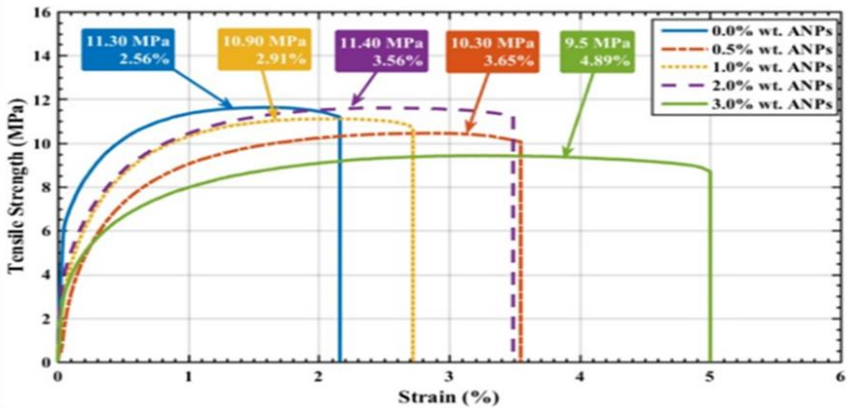

(a) NCPC incorporating ANPs stress-strain curves for tensile test.

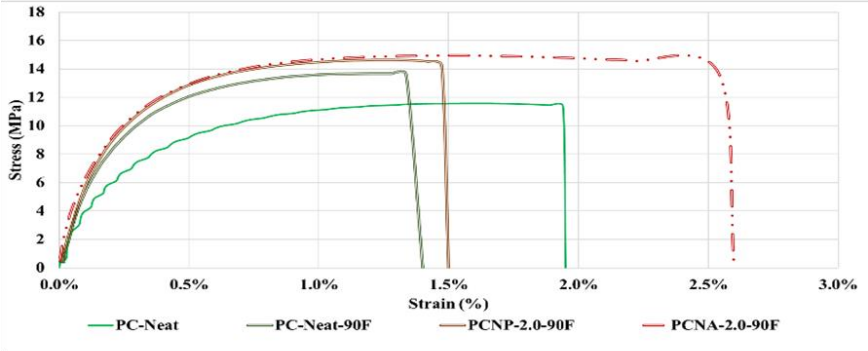

(b) NCPC at 90% filler content incorporating P-MWCNTs and ANPs.

Figure 10: Stress-strain diagrams for NCPC mixes in tensile test.

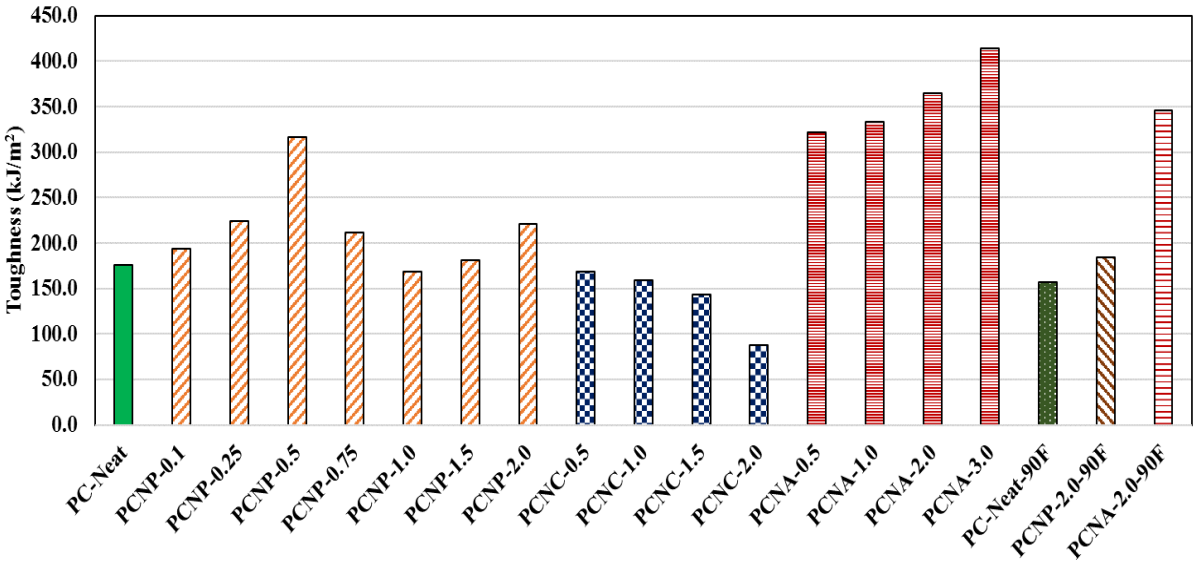

Figure 11: Toughness of PC and NCPC in tensile test.

NCPC mixes containing 100% filler:

The results above show evidently nominal curing conditions for the PC samples at 60℃. All mixes reached sufficiently high tensile strength with a maximum of 11.30 MPa for PC-Neat. Such tensile strength is significantly higher than that of ordinary concrete (OC) and ordinary cementitious materials used in construction. OC samples will be prepared for comparison at a later stage. The addition of nanomaterials showed a change of tensile strength in the range of -5% to -22% for P-MWCNTs, -8% to 36% for COOH-MWCNTs, -4% to -16% for ANPs. Mixes containing P-MWCNTs content ≤ 0.5 wt.% showed larger drop than those of higher contents. COOH-MWCNTs samples were the only samples to show improvement of tensile strength at 1.5 and 2.0 wt.% content. This is attributed to the functionalization of MWCNTs that enables nanotubes to perform chemical bonds with the host polymer matrix. The tensile strength of ANPs mixes decrease similarly to P-MWCNTs with slightly less decrease from that of nanotubes. Nonetheless, the tensile strength of all NCPC is significantly higher of OC at the range of 9-15.4 MPa. On the other hand, improvements in strain at failure and toughness were observed due to the incorporation of nanomaterials. Specifically, samples containing 3.0 wt.% ANPs content reached 4.9%. P-MWCNTs showed two distinct behaviors however at contents ≤ 0.75 wt.% compared higher contents. At low contents, the tensile strain at failure was firmly in the range of 2.3-2.9% with no clear impact of the content of nanotubes. At 1.0 wt.% content, the strain at failure drops from that of lower contents to 1.6%. The addition of higher contents of nanotubes then corresponds to improvement in tensile strain. In fact, at 2.0 wt.% content, NCPC shows similar strain at failure of that of lower contents. In contrast, mixes containing COOH-MWCNTs shows a decrease of tensile strain at failure with the increase in content. This is in agreement with the findings of tensile strength as higher content results in increased reactivity increasing the crosslinking of the polymer. Nonetheless, appreciable strain is achieved in the range of 0.8-1.9%. Therefore, it's evident that the addition of nanomaterials significantly increase the ductility of PC.

To further investigate the ductility, the area under the stress-strain curves of the tension test were measured representing toughness. Significant increase is observed for all mixes ranging from -4% to 80% for P-MWCNTs, -50% to -4% for COOH-MWCNTs, and 83% to 135% for ANP. P-MWCNTs results showed trends similar to those found in the results of strain at failure. However, at 0.1 wt.% content the increase in toughness is significantly different that those at contents in the range of 0.1-0.75 wt.%. At 1.0 wt.% the toughness is lower than that at lower content but a general increase is observed with the increase of content up to 2.0 wt.% content where it reaches similar increase to that observed at lower contents. Mixes incorporating COOH-MWCNTs showed a decrease in toughness with the increase in content of nanotubes. These results agree with the findings of strength and strain at failure confirming the increase in cross linking. 3.0 wt.% content of ANPs provides the highest increase in toughness and strain at failure.

Microstructural investigation is aimed to explain the differences in findings for all nanomaterials used.

NCPC mixes containing 90% filler:

The reduction in filler content resulted in an increase in tensile strength by 21%, decrease in strain at failure by -52% and a decrease in toughness by -11%. This is explained by the increase in the crosslinking of the polymer chains that are less interrupted with lower content of aggregate filler. Also, the decrease in filler content results in an increase in particle density distribution eliminating part of the larger particles. Therefore, the results with 90% filler showed demolished effect of nanomaterials on PC-Neat when compared to 100% Filler. Tensile strength increased by 7% and 10% for P-MWCNTs and ANPs at 2.0 wt.% content respectively. While the effect of P-MWCNTs on strain and displacement is insignificant, ANPs had showed low increase in strain and displacement by 51% and 10% when compared with PC-Neat-90F. The change in toughness is also negligible for P-MWCNTs with an increase of 18% but more significant with ANPs at 120%. As mentioned earlier, the effect of nanomaterials at 90% filler is demolished as moving the increase in toughness, for example, from 550% to 120% for ANP.

Compression Testing

Compressive testing of PC and NCPC was performed using 2inØ x 4 in cylinders. Samples were casted and cured in similar fashion to tension samples using 60℃. Testing of PC showed significant deformation prior to reaching the compressive strength of the samples as shown in **Figure 12**. **Figure 13** shows the compressive strength of all mixes discussed previously in the tension testing section. At 100% filler, the inclusion of nanomaterials decreases the compressive strength of PC-Neat by 18% and 22% for MWCNTs and ANP. On the other hand, at 90% filler, the compressive strength for the mixes incorporating MWCNTs and ANPs showed an increase of 35% for both.

Figure 12: Compression cylinders: Tested sample (right) with untested (left).

It seems the effect of nanomaterials on the materials strength (in compression or tension) is reduced by the addition of nanomaterials. However, the strain of the material is significantly improved. At lower content of filler, the effect of nanomaterials in improving ductility is decreased but strength is gained. The percentage of tensile strength to compressive strength of PC and NCPC seems significantly different of that of OC. **Figure 14** shows such relationship PC and NCPC tensile capacity is significantly close to its compressive strength. Nanomaterials improve the tensile capacity of PC more significantly than its compressive strength. Therefore, the percentage of tensile strength to compressive strength for both neat samples is higher than that of NCPC. Future work will discuss different curing conditions, filler content and nanomaterials percentage incorporated as well OC testing to correlate the results of PC-Neat.

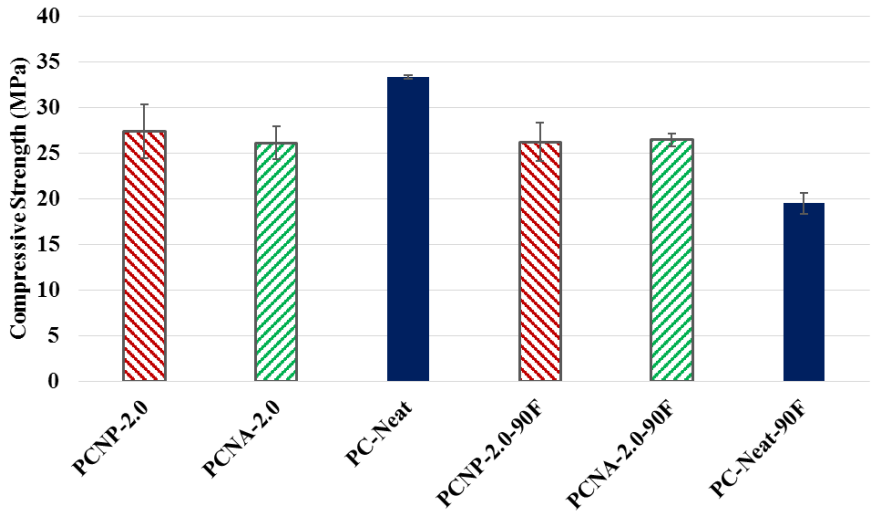

Figure 13: Compressive strength of PC and NCPC.

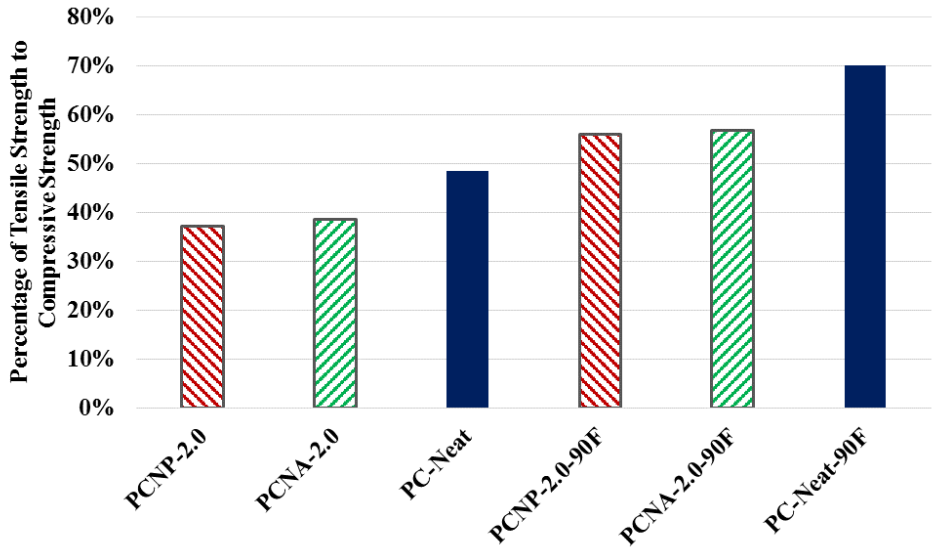

Figure 14: Percentage of tensile strength to compressive strength of PC and NCPC.

Electrical Monitoring and Damage Feature

Electrical conductivity measurement was recorded for PCNP-2.0 to PCNP-3.0 and damage feature λ(t) was calculated using **Equation 1**. The damage feature λ(t) represents the change in electrical resistance with $R(t)$ and $R(t_0)$ as the electrical resistance of the PC beam at time t and t_0. A quantification of the mechanical damage evolution was performed for all tests through measurements of the change in flexural rigidity. Equation 2 and 3 show the details of this measurement. where *EI(i)* is the specimen flexural rigidity at any cycle, *E* is the modulus of elasticity, *I* is the cross sectional second moment of inertia, $\Delta P(i)$ is the difference between maximum and minimum loads at the same cycle, $\Delta\delta(i)$ is the corresponding difference between displacements, *L* is the span length of 175 mm, *D(i)* is the fatigue damage in %, and *EI(0)* is the initial flexural rigidity.

$$\lambda(t) = \frac{R(t) - R(t_0)}{R(t_0)} \quad (1)$$

$$EI(i) = \left(\frac{5}{288}\right) * \frac{\Delta\,\mathrm{P(i)} * \mathrm{L\hat{}3}}{\Delta\,\delta(\mathrm{i})} \quad (2)$$

$$D(i) = 1 - \frac{EI(i)}{EI(0)} \quad (3)$$

However, the resistance of Neat, PCNP-0.5 and PCNP-1.0 were too low to record conductivity/resistivity changes quantifying damage during flexural testing. However, by incorporating 2.0 wt.% MWCNTs the change in electrical resistance of the PC beams was successfully recorded with a typical source meter. However, it is worth noting that NCPC-3.0 with 3.0% P-MWCNTs was challenging to produce due to the significantly

high viscosity. Nonetheless, PCNP-2.0 and PCNP-3.0 provided sufficient damage monitoring. The increase of load during static flexural loading corresponds to an increase in microcrack development at the interface and then within the matrix. Such cracks are then intersected by the high content of well-dispersed MWCNTs. This is shown by an increase in resistivity of the PC beam with the increase in load. **Figure 15** shows the test set-up used for monitoring damage propagation in PC under static loading. **Figure 15** also depicts the superior ductility/deformability of PC incorporating MWCNTs (this case for 2.0% P-MWCNTs). **Figure 16 and 17** show the relationship between the load-damage feature λ(t) and load-displacement of PCNP-2.0 and PCNP-3.0 respectively. It is evident incorporating P-MWCNTs in PC matrix prior to fabrication allows monitoring damage evolution during static flexural loading to failure.

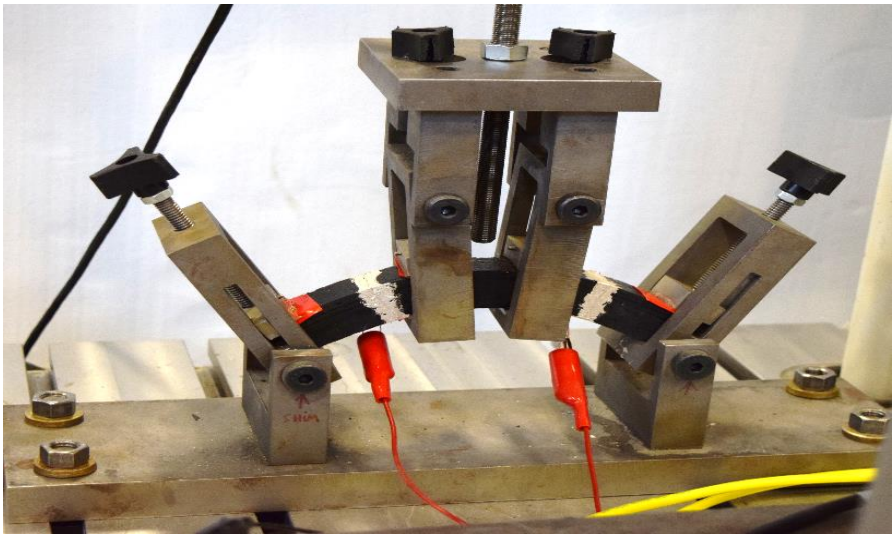

Figure 15: Test set-up for monitoring damage evolution in PC under flexural static loading. Figure shows the extreme deformability of PC incorporating P-MWCNTs. Red connectors are connected to silver tape painted on around PC to measure change in electrical resis

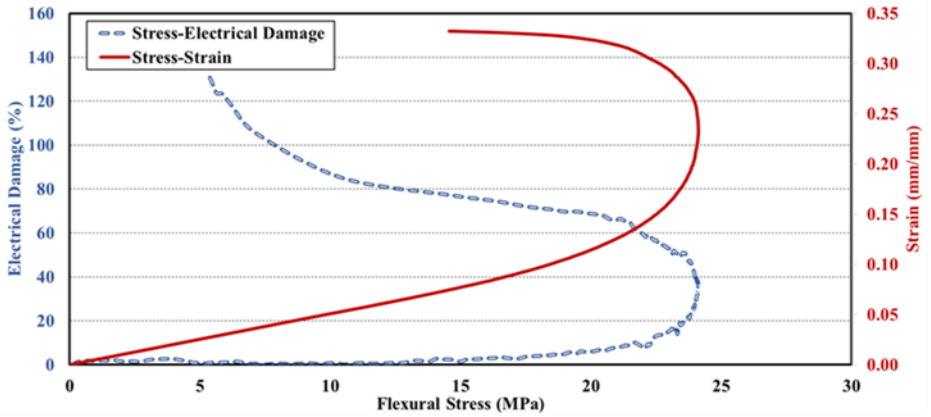

(a) Electrical damage feature vs flexural stress and stress-strain for PCNP-2.0

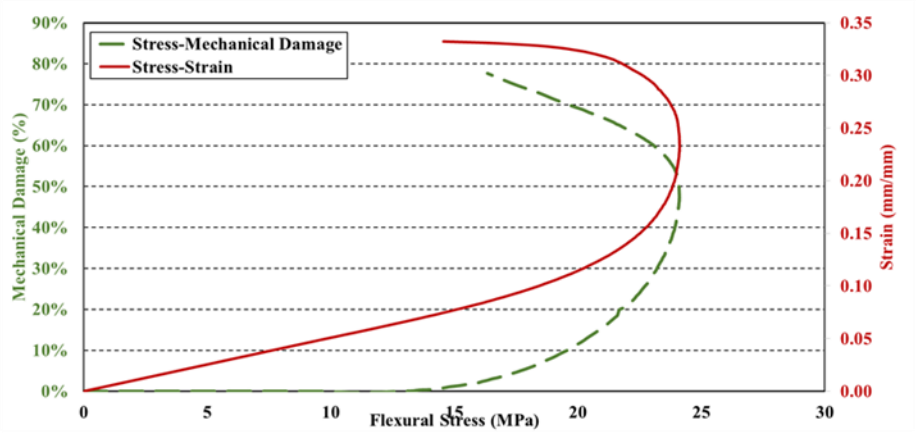

(b)Mechanical damage evolution vs flexural stress and stress-strain for PCNP-2.0

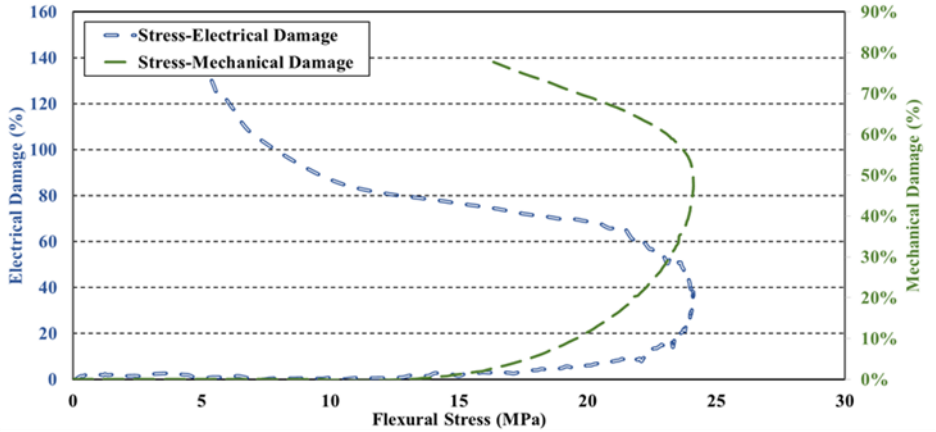

(c) Electrical damage feature vs flexural stress and mechanical damage evolution vs flexural stress for PCNP-2.0

Figure 16: Electrical damage, mechanical damage and strain with respect to stress for PCNP-2.0 showing the ability of monitoring static damage evolution in PC with MWCNTs using electrical conductivity.

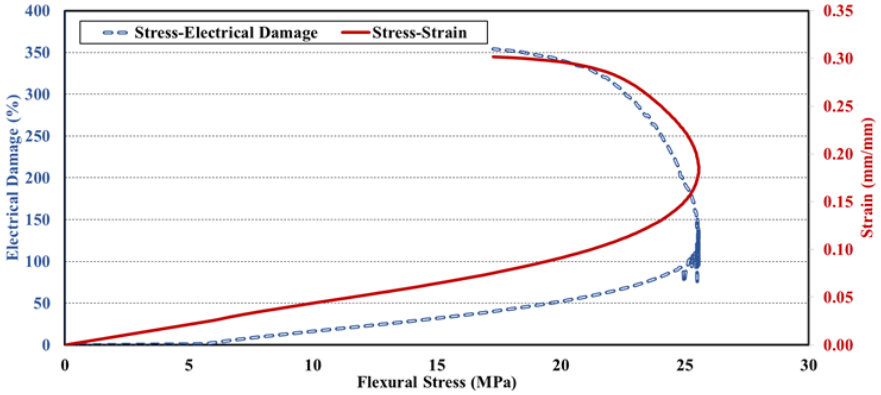

(a) Electrical damage feature vs flexural stress and stress-strain for PCNP-3.0

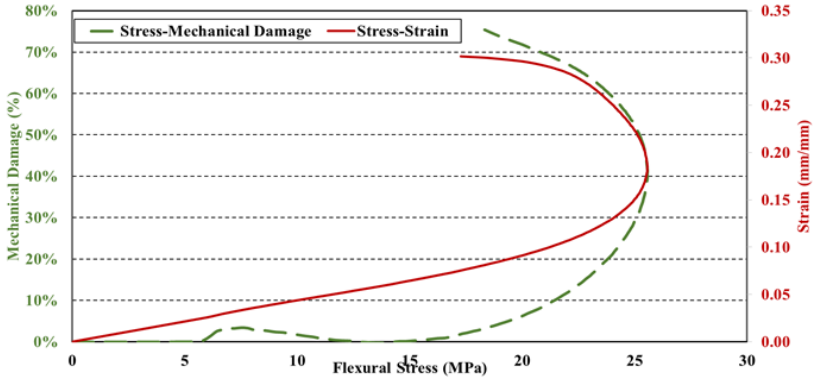

(b) Mechanical damage evolution vs flexural stress and stress-strain for PCNP-3.0

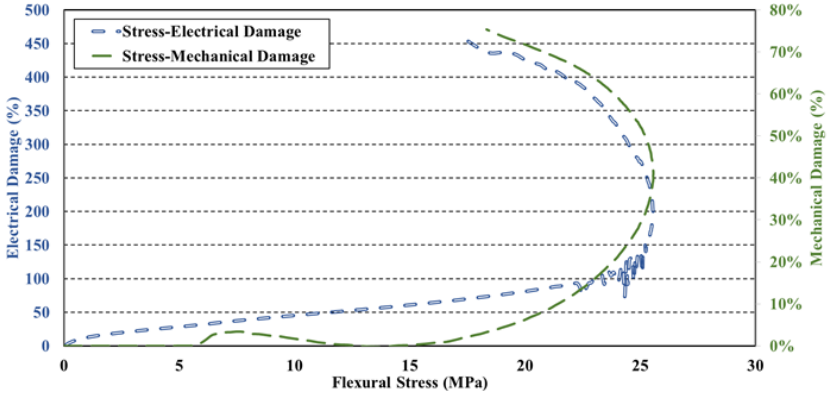

(c) Electrical damage feature vs flexural stress and mechanical damage evolution vs flexural stress for PCNP-3.0

Figure 17: Electrical damage, mechanical damage and strain with respect to stress for PCNP-3.0 showing the ability of monitoring static damage evolution in PC with MWCNTs using electrical conductivity.

Fatigue testing of PC overlays with and without nanomaterials

There is no standard fatigue test for concrete. This is attributed to the difficulty to conduct the fatigue test on concrete with repeatable results. We therefore suggest borrowing the standard fatigue test for asphalt overlay AASHTO T321- 07 [61] and modifying it to allow testing of the PC overlay. The fatigue test proposed is a four-point bending displacement controlled cyclic test. In this test, the displacement will be ramped up from zero to 2.0 mm in 1 minute, then test specimens will be cycled between 1.0 and 2.0 mm using a sinusoidal waveform with a frequency of 1.0 Hz. Five prisms of each mix will be tested. Each prism is 25 x 25 x 200 mm. The test will be conducted on an MTS® Bionix servo hydraulic system in the PI's lab (please see facilities section). A new test fixture has been designed and produced by the PI as shown in **Figure 18**. The new set-up allows holding two linear variable differential transducers (LVDTs) at the centre line of the test specimen in order to record the displacement. Through the test, time, load and displacement will be recorded and at a sampling rate of 10 Hz. The recorded time (number of cycles), load and displacement will allow for determining the fatigue strength and damage propagation in the specimen. Following the AASHTO standard [61], failure point is considered when the cycle experienced 50% reduction in the initial flexural rigidity.

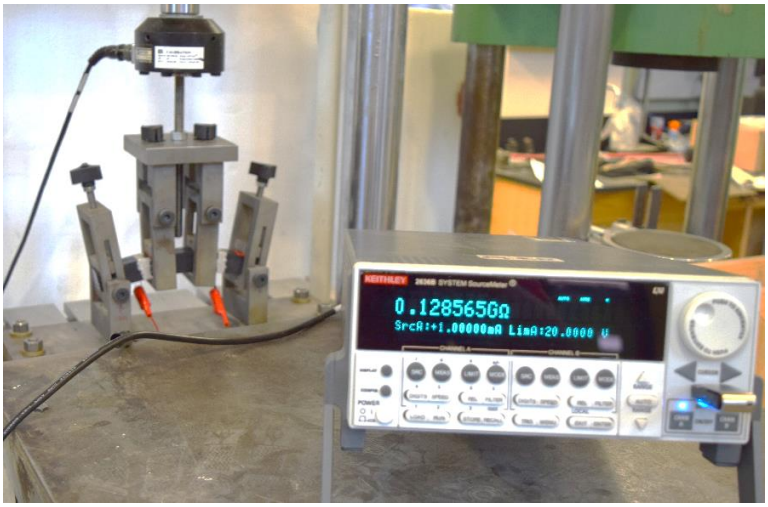

Figure 18: New fatigue test set-up developed by the PI showing the loading frame and the source meter connected to measure change in electrical resistance to monitor fatigue damage evolution in PC.

Testing showed that incorporating MWCNTs can significantly improve the electrical conductivity of PC and thus enabled monitoring fatigue damage propagation in PC. **Figure 19** shows an example result for monitoring fatigue damage as the change in electrical resistance in PC. It is interesting to note the significant improvement of PC fatigue life incorporating 1.0% MWCNTs increased fatigue life of PC under the same cyclic loading from 75,000 cycles to 300,000 cycles representing 300% increase in

fatigue life of PC. It is also apparent that the change in electrical conductivity/resistivity follows the classical damage propagation modes of initial, steady-state to tertiary confirming the ability of the proposed technique to monitor damage propagation in PC. We note that measurements of PC incorporating less than 2.0% MWCNTs did not show improvement of electrical conductivity. Further testing by the PIs confirmed that 2.0% to be the percolation limit for this type of MWCNTs.

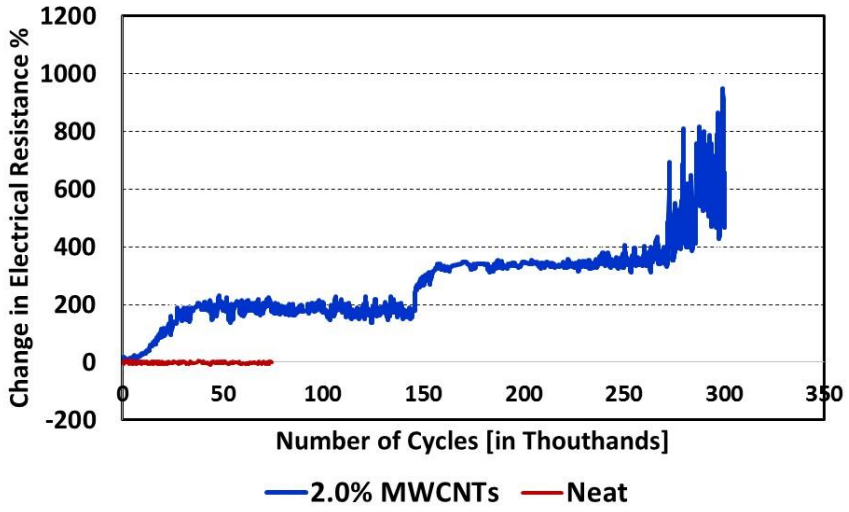

Figure 19: Change in electrical resistance in PC with and without MWCNTs. Figure shows the non-conductive nature of PC neat and the ability to measure electrical conductivity of PC incorporating 2.0% MWCNTs.

Test results of PC-Neat, PCNP-0.5, PCNP-1.0, PCNP-2.0 and PCNP-3.0 showed an increase in number of cycles to failure criteria described previously (50% reduction in initial flexural rigidity) by incorporating MWCNTs. Fatigue life test results are presented in **Figure 20**.

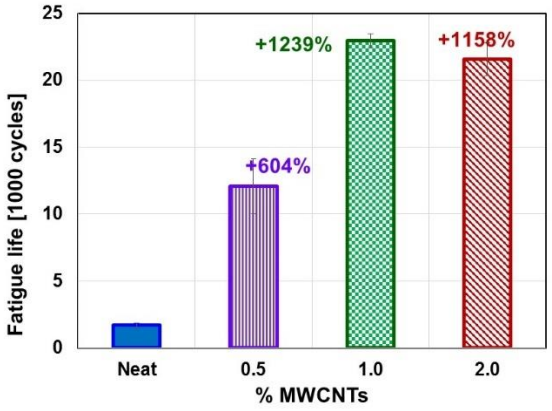

Figure 20: Fatigue life of PC incorporating MWCNTs showing the increase of fatigue life for PC incorporating 1-2% MWCNTs. (% values above bars represent change compared with neat PC).

Fracture toughness testing of PC overlays with and without nanomaterials

Fracture toughness of PC with and without nanomaterials was determined using four-point bending. The test set-up developed is a notched beam test to obtain a bilinear approximation of the complete stress-crack opening displacement (COD) curve following the procedure presented in ACI 446 [62], which follows the original work of Guinea et al. [63]. In this test a beam is notched and is loaded in three-point bending and feedback is provided using Crack Mouth Opening Displacement (CMOD) measurement. Load rates were determined through trial testing with based on displacement control samples to ensure reaching the peak in timely fashion and record the softening curves of the tested specimen. ACI 446 [62] provides a detailed description of the test specimen preparation, loading set-up and test procedure. A standard beam 25 x 25 x 150 mm test is used. The test enables extracting standard stress-COD curves and thus fracture toughness K_{IC} and fracture energy G_F. All this information is essential for predicting fatigue strength of PC and for modeling PC.

Two setups were used in executing the four point bending tests. **Figures 21** and **22** show the initial and the final setups with proof of the excessive deformation leading to developing the new setup. Due to the ductile nature of PC and the extensive displacement and CMOD exhibited with cracking, special clip gauge was also used to capture CMOD values up to 14 mm. The initial setup used allowed confirmation of capturing the fracture toughness parameters of PC with four-point bending. The new setup had to be developed to capture the significant deformations as well as the effect of the large fracture process zone. The new setup confirms to ACI 446 recommendations on the fracture testing of concrete as well as it adapts to the ductile nature of PC. **Figure 23** shows the schematics of all the parts and design drawings of the new setup. The new setup allows for testing different fracture samples at different lengths. This allows the PI to produce samples with overhangs that counter the self-weight; hence, eliminating the moment at the crack location. The new fixture also allows the rotation of one of the supports and the loading heads with $\pm 10°$. The new fixture drawings are shown in **Figure 24**.

Figure 21: Initial load setup by the PI to examine the fracture toughness of PC

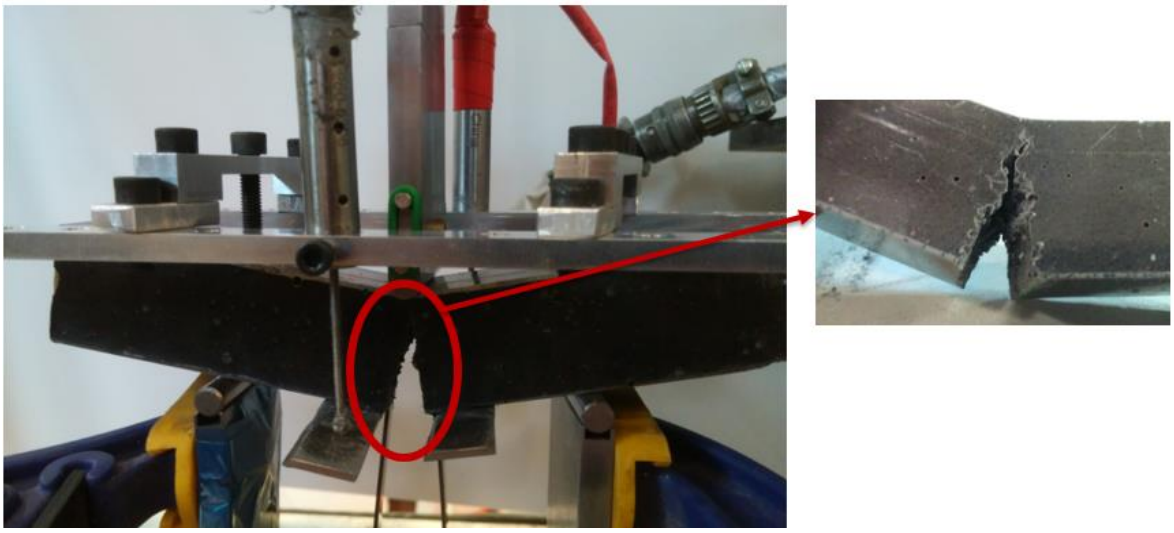

Figure 22: Modified fracture toughness test setup per ACI446 used to capture all tests.

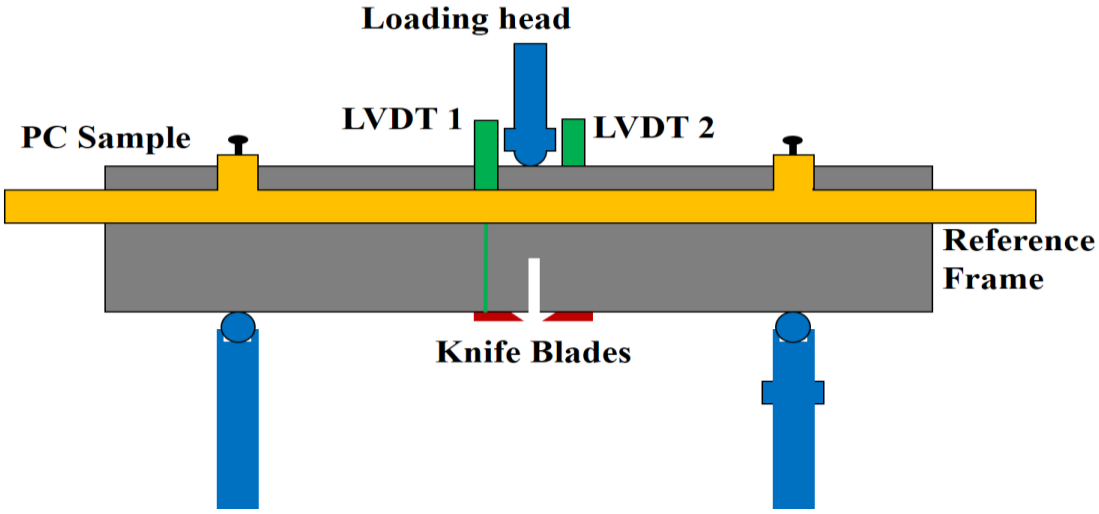

Figure 23: Schematics of the setup presented in Figure 21 clarifying all test features.

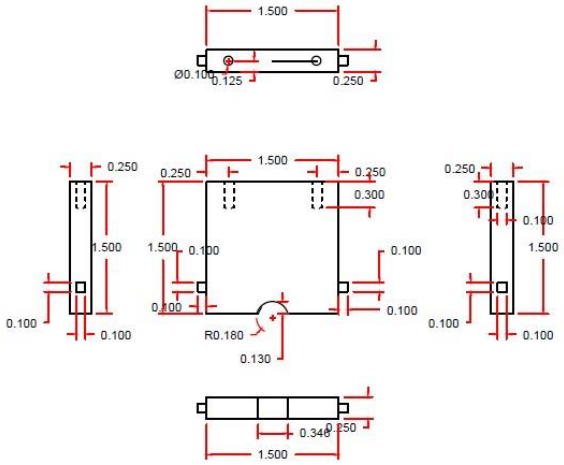

(a) Loading head: Top part

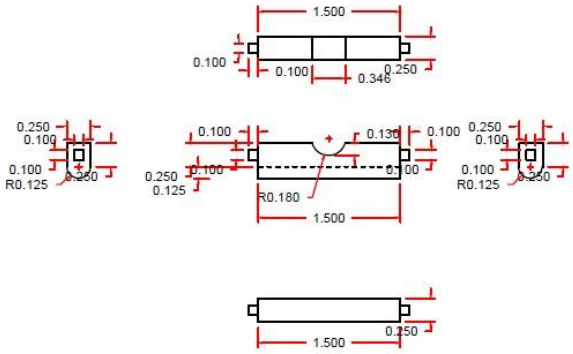

(b) Loading head: Bottom part

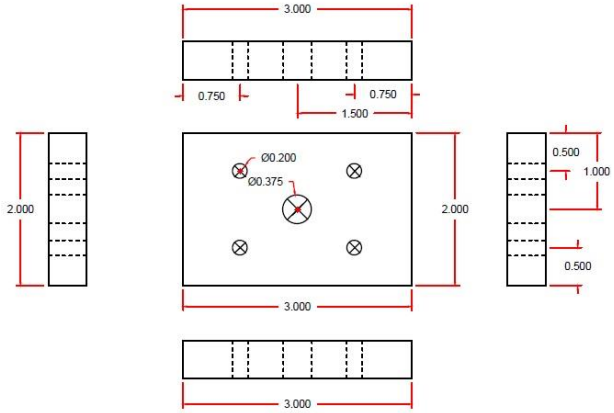

(c) Loading head: Loading plate

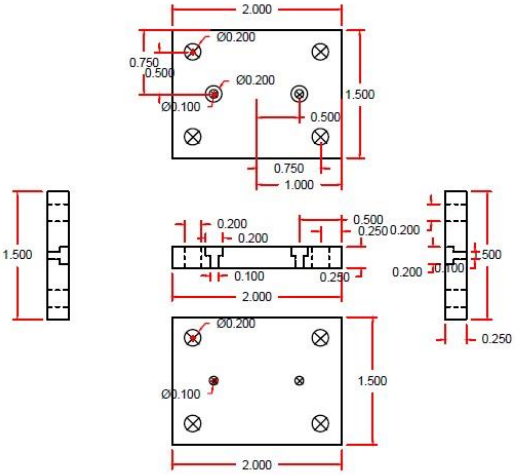

(d) Loading head: Intermediate plate

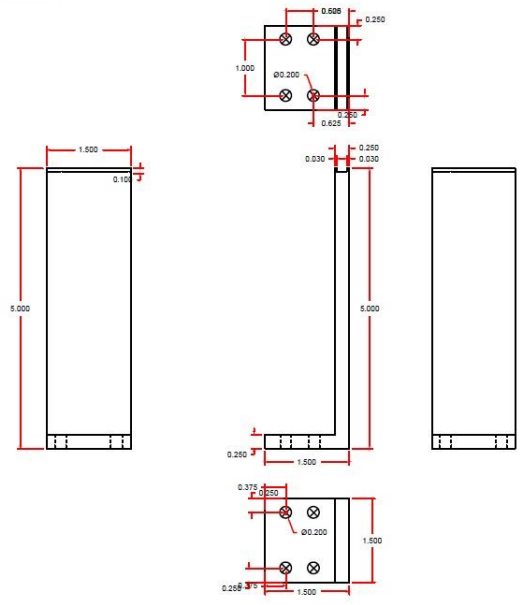

(e) Loading frame: Left support

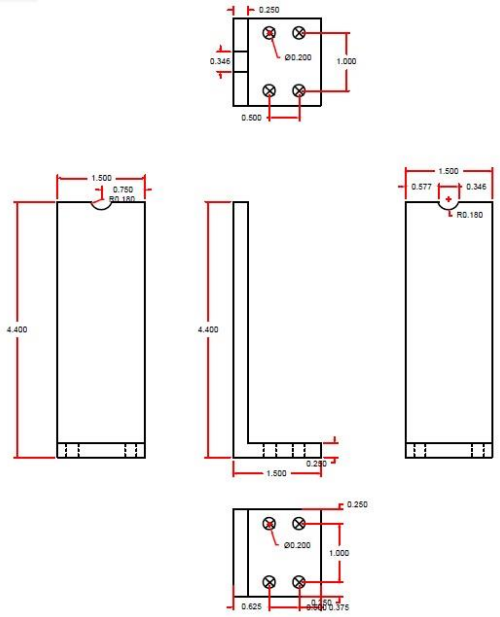

(f) Loading frame: Right support

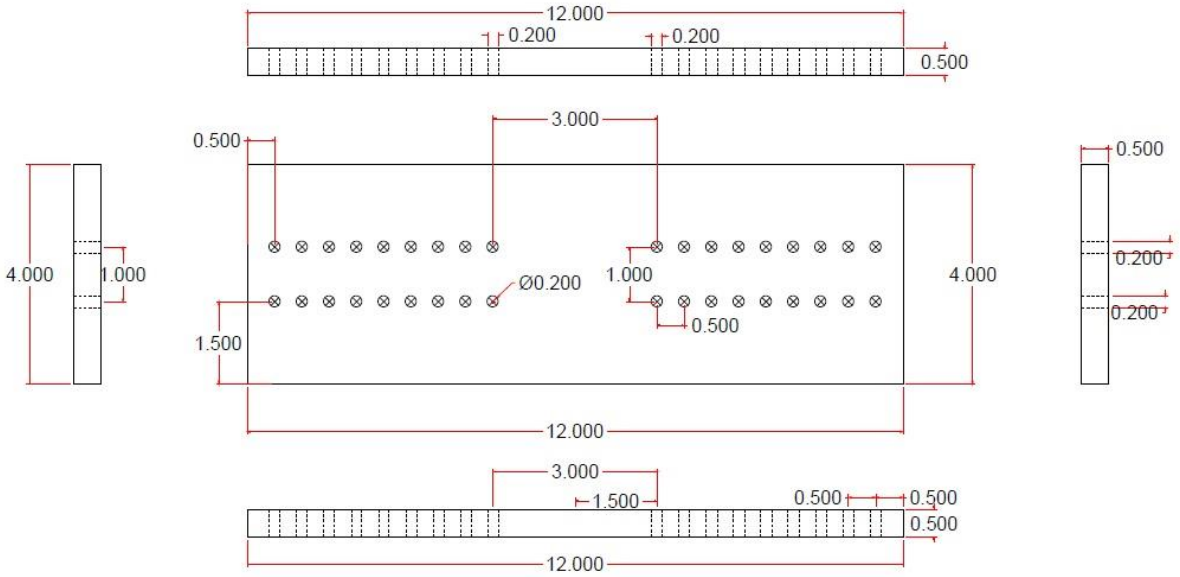

(g) Loading frame: Loading plate

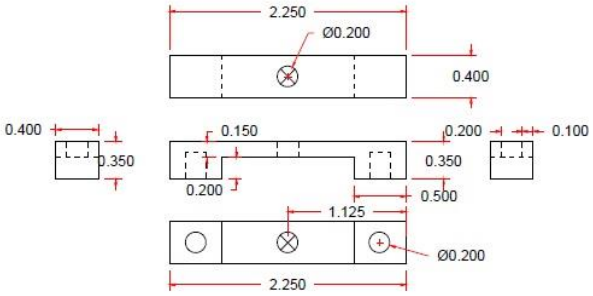

(h) Reference frame: Top part – First support

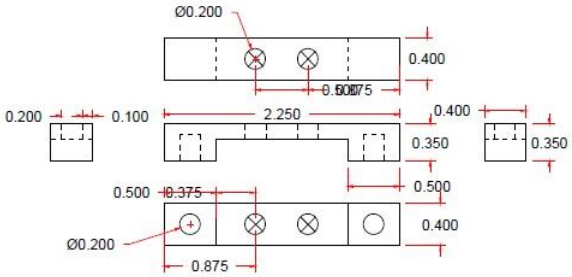

(i) Reference frame: Top part – Second support

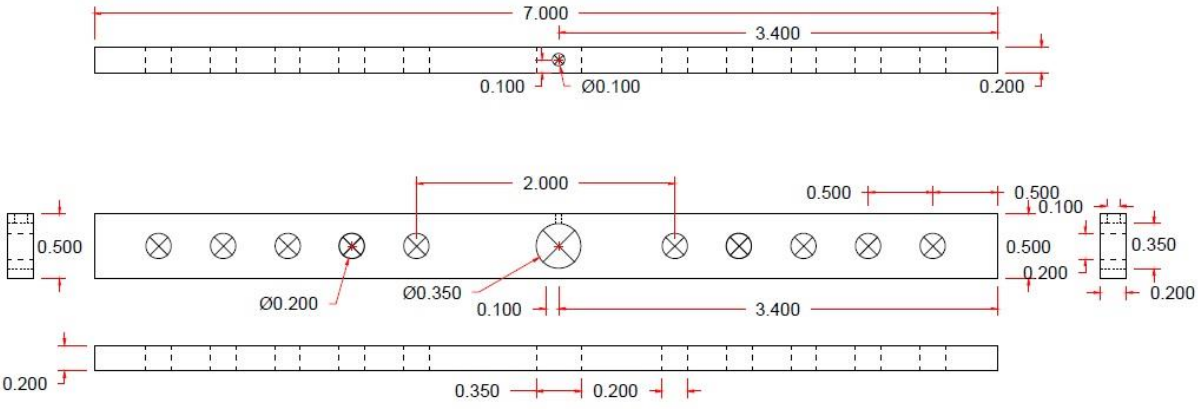

(j) Reference frame: Bottom part

Figure 24: Shop drawings for fracture test setup including loading and reference frames.

Analysis of the data was based on work by Guinea et al. [63] and Chapman [64] for using principles of LEFM to identify the bilinear stress-COD curves and thus fracture

toughness K_{IC} and fracture energy G_F. Principles of this analysis are presented in **Figures 25** and **26** and are summarized by Equations (4) to (8). With all variables defined in **Figure 23**. Sensitivity analysis was conducted to identify the cut-off limit of the asymptotic part of the load-CMOD curves to accurately determine the fracture toughness of PC with and without P-MWCNTs when using LEFM. The results are then used to confirm the application of LEFM and determine the accuracy of method of analysis.

$$d = \frac{S * w_c}{4\,\delta} \tag{4}$$

$$T = B \int_{z=0}^{d} f\big(w(z)\big) dz \tag{5}$$

$$\frac{S}{4}\left(P + \frac{mg}{2}\right) = K_0\, Td \qquad \text{as} \quad P(\delta) = P + \frac{mg}{2} \quad \text{thus} \quad \frac{P(\delta)S}{4} = K_0\, Td \tag{6}$$

$$T = B \int_{w=0}^{w_c} f(w) \frac{d}{w_c} dw \quad \text{and} \quad G_F = \int_{w=0}^{w_c} f(w)\, dw \quad \text{thus} \quad T = \mathrm{dB}\frac{G_F}{w_c} \tag{7}$$

$$P(\delta) = \frac{1}{4} BSK_0\, G_F w_c \tag{8}$$

With B, S, K_0, w_c being constants for an LEFM material, the fracture toughness G_F can be determined based on the load value $P(\delta)$ occurring when the COD reaches it critical value w_c.

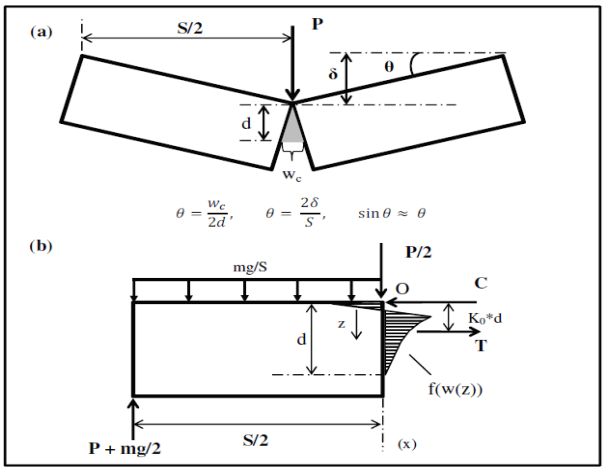

Figure 25: Basic principles used for analysis of notched beam set-up data to extract the bilinear fracture curve of PC after Chapman [64].

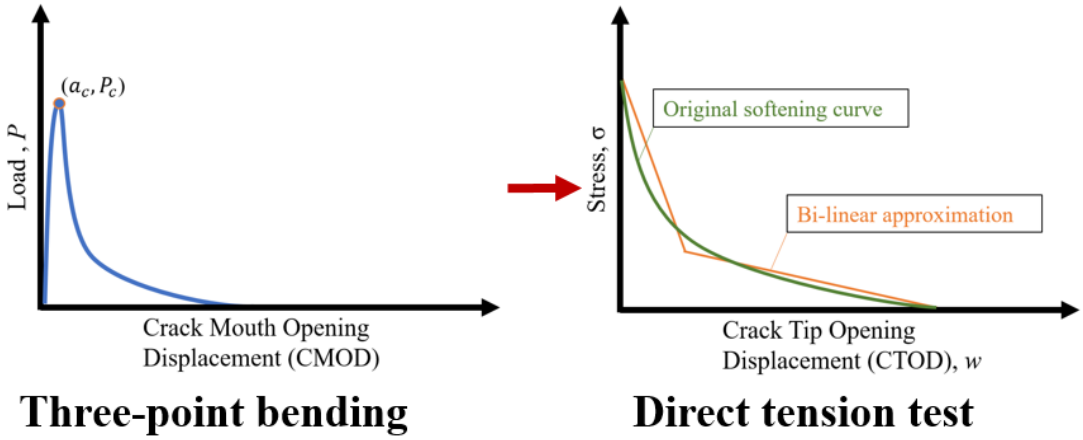

Figure 26: Schematics of the methods prescribed to translate the test data from three-point bending to direct tension test as prescribed by Chapman.

Results of load-CMOD curves are shown in **figure 27** for samples containing 0.5, 1.0, 1.5 and 2.0 wt.% MWCNTs and Neat Namely PCNP-0.5, PCNP-1.0, PCNP-1.5, PCNP-2.0 and PC-Neat respectively. The bilinear approximation curves generated per the previous discussion are shown in **figure 28**. Analysis of those curves allowed the calculation of the fracture toughness parameters and evaluate the effect of incorporating MWCNTs. Those results show a general increase in the fracture toughness of PC due to the incorporation of MWCNTs in the range of 24-73% as shown in **figure 29**. Tension tests allowed the extraction of the modulus of elasticity and the yield strength of PC. Two parameters that along the fracture toughness are needed to confirm the applicability of LEFM analysis. Equation (9) was used to measure the analysis's least sample dimension required for LEFM analysis and the results are shown in **table 2**.

$$l \geq 2.5\left(\frac{K_{1C}}{\sigma_y}\right)^2 = 2.5\left(\frac{\sqrt{G_F E}}{\sigma_y}\right)^2 \quad (9)$$

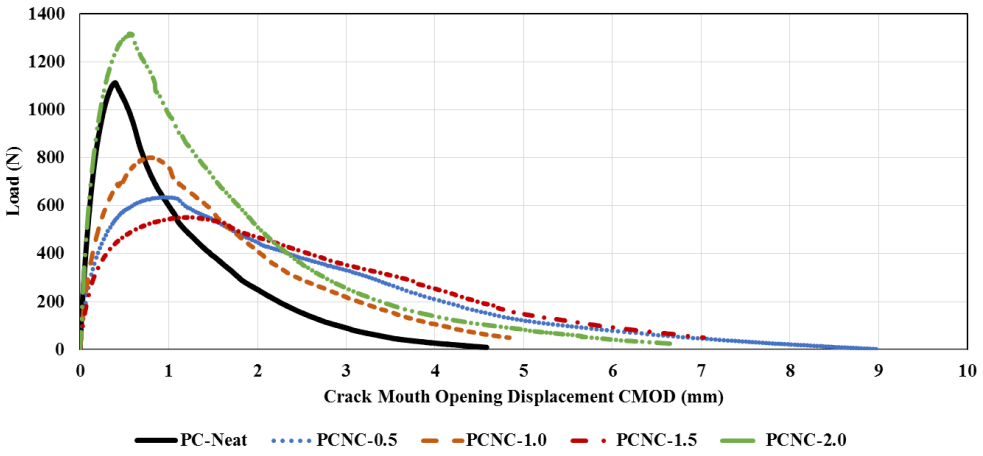

Figure 27: Load-CMOD curves for PC samples with and without MWCNTs.

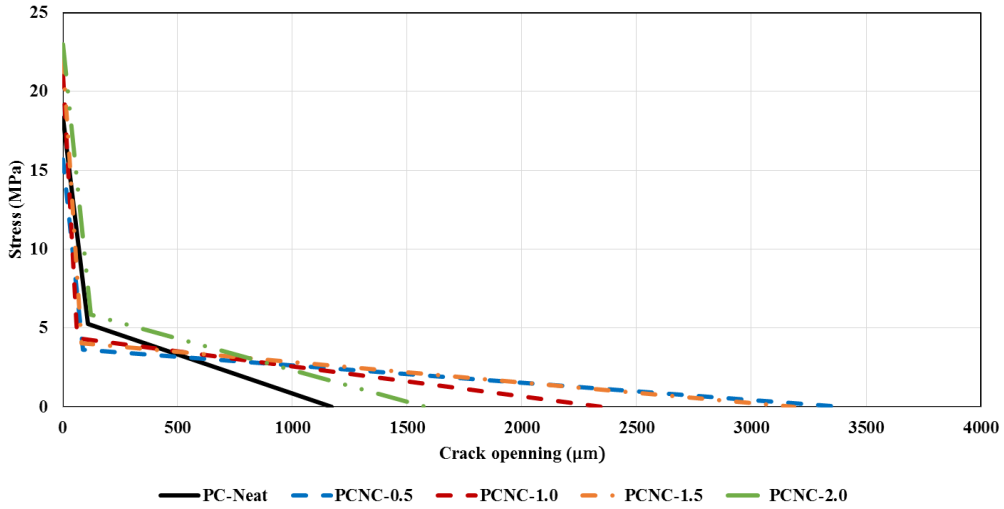

Figure 28: Schematics of the methods prescribed to translate the test data from three-point

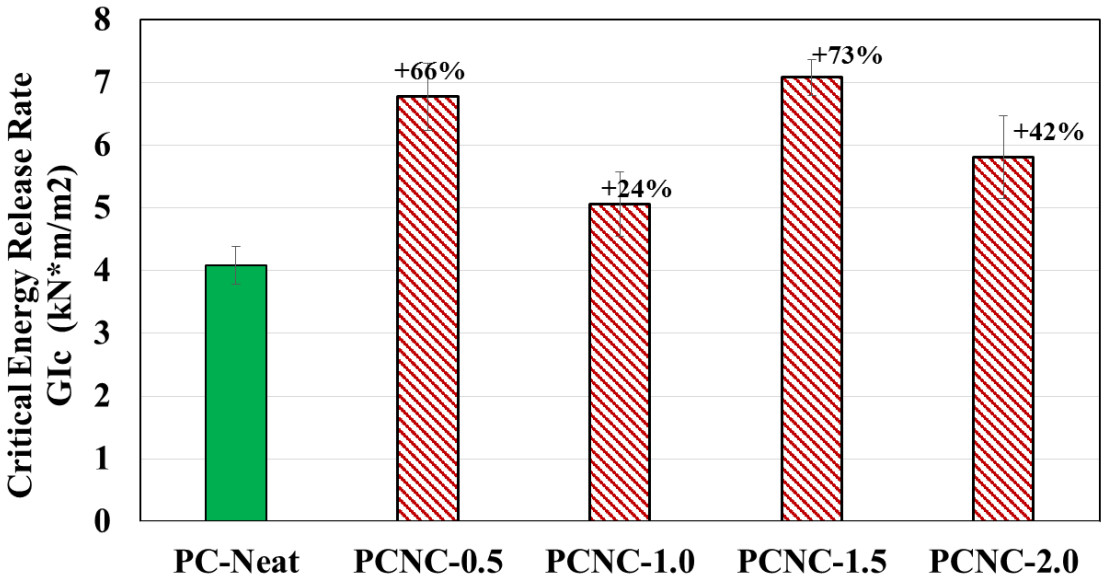

Figure 29: Schematics of the methods prescribed to translate the test data from three-point

Table 2: Linear elastic fracture mechanics least dimension parameter values.

Value	PC-Neat	PCNP-0.5	PCNP-1.0	PCNP-1.5	PCNP-2.0
E (GPa)	14.2	6.07	11.2	9.37	5.53
G_F (kN/m)	4.09	6.77	5.06	7.08	5.80
σ_y (MPa)	16.1	8.9	10.7	10.6	10.2
***l* (mm)**	560	1287	1231	1490	772

The previous shows that LEFM is not an applicable analysis method since the least sample's dimension is 8 mm (representing the length of the crack) which is an order of magnitude lower than the limit discussed in **table 2**. Hence, it was confirmed that PC with and without MWCNTs exhibit Quasi-Brittle like material behavior and requires further investigation to better quantify their fracture toughness parameters. The effective crack modulus method of analysis was chosen based on prior work by the PI on Quasi-Brittle Fracture Mechanics (QBFM) analysis [65]. This method of analysis was selected due to the presence of large fracture process zone in which it increases the consumption of fracture energy as shown in **figure 30** and equation (10). Equations (11) and (12) describe the effective elastic modulus of both the elastic and the critical limits respectively. Equations (11) and (12) were used in support with (13) - (18) to calculate all other parameters. A total fracture energy (T_{Ic}) was introduced per equation 19 that combines the fracture energy from both the J-integral and the energy release rate. **Figure 31** shows the for-loop process performed on a Matlab code to determine the critical crack depth used to measure QBFM fracture toughness parameters.

$$G_I = G_{Ic} + \int_0^{CTOD_c} \sigma(CTOD)d(CTOD) \tag{10}$$

$$E^* = \frac{1}{bd\delta_c}\left(\frac{13wl^4}{32d^2} + \frac{3P_c l^3}{4d^2} + \frac{3(1+v)P_c l}{4} + \frac{9P_c l^2}{2d}F(\alpha_{ic})\right) \tag{11}$$

$$E = \frac{1}{bd\delta_e}\left(\frac{13wl^4}{32d^2} + \frac{3P_e l^3}{4d^2} + \frac{3(1+v)P_e l}{4} + \frac{9P_e l^2}{2d}F(\alpha_{ie})\right) \tag{12}$$

$$F(\alpha_i) = \int_0^{\alpha_i} \alpha\, g^2(\alpha)d\alpha \tag{13}$$

$$g(\alpha) = g_1(\alpha)\sqrt{\pi}\,, \alpha = \frac{a}{d} \tag{14}$$

$$g_1(\alpha) = 1.122 - 1.4\alpha + 7.33\alpha^2 - 13.08\alpha^3 + 14.0\alpha^4 \quad (15)$$

$$K_I = g_1(\alpha)\sigma\sqrt{\pi a} \quad (16)$$

$$G_{Ic} = \frac{K_{Ic}^2}{E} \quad (17)$$

$$J_{Ic} = \frac{2}{H_c b}(A_N - A_{UN}) \quad (18)$$

$$T_{Ic} = G_{Ic} + J_{Ic} \quad (19)$$

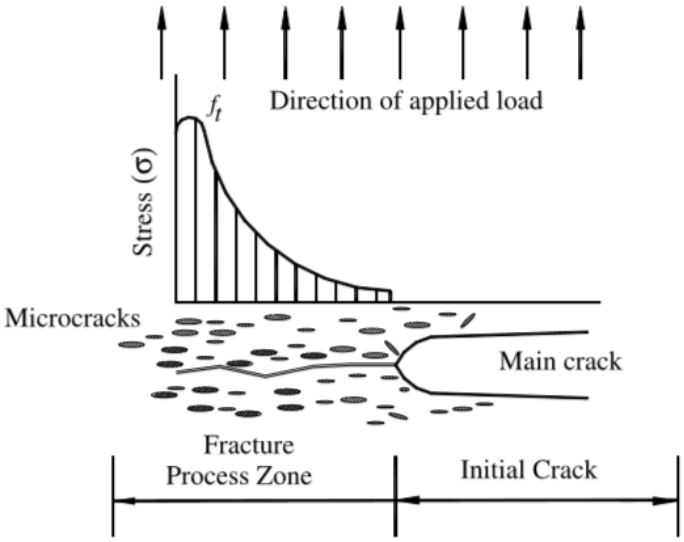

Figure 30: Model of Quasi-Brittle Fracture materials showing the increase in stress due to the fracture process zone [66].

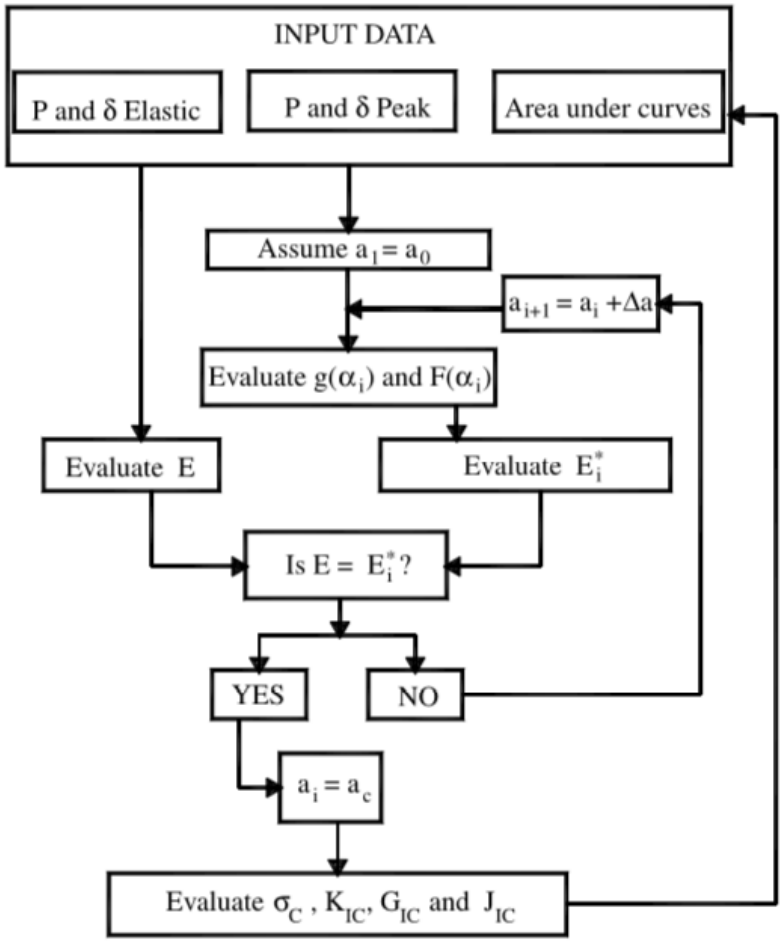

Figure 31: QBFM analysis for-loop using the effective crack modulus [65].

The results of QBFM analysis are presented according to the three different material parameters as shown in **figures 32 – 35**. The fracture toughness parameters per QBFM define the fracture toughness energy to be of two parts: one consumed through elastic deformation creating new surfaces and another consumed at the fracture process zone. Those parts present the LEFM and J-integral parameters. Hence, the combination of those two parameters determine the effect of nanoparticles on the fracture toughness. **Figure 32** shows the effect of all nanoparticles at different contents on the critical stress intensity factors (K_{Ic}). P-MWCNTs showed a change in the range of -6% to 20%, COOH-MWCNTs showed an increase of 21% to 39% and ANPs showed -14% to 155%. However, the effect of nanoparticles on such parameter don't provide the complete effect of quasi-brittle materials and the effect on energy consumption is the critical parameter. **Figures 33-35** display the effect of each nanoparticle on the energy release rate. Specifically, **Figure 35** shows the total effect while **figures 33** and **34** show the components in which each nanoparticle at specific content provides improvements. For P-MWCNTs, two different behaviors appear as discussed previously with tension results. At 0.5 wt.% content, a total improvement of 56% is achieved strictly from J-

integral energy. At 1.0 wt.%, the results show that the total fracture energy is reduced by 31%. This reduction is greatly affected by the critical energy release rate rather than J-integral. At 1.5 wt.% content, similar reduction in critical energy release rate is observed but with rather significant improvements in the J-integral values resulting in a total increase in total fracture energy of 52%. At 2.0 wt.% content, the reduction in critical energy release rate is diminished while maintaining significant improvements in J-integral netting a 47% increase in total fracture energy. Therefore, P-MWCNTs improve the fracture toughness of PC at 0.5, 1.5 and 2.0 wt.% with 47% to 56% while at 1.0 wt.% decrease the fracture toughness with -31%. COOH-MWCNTs on the other hand follow mostly a consistent pattern between their content and their impact on fracture toughness up to 1.5 wt.%. The increase in total fracture energy decrease from 112% at 0.5 wt.% to 64% at 1.5 wt.%. at 2.0 wt.% content the total fracture energy increase again by 81%. The increase in fracture toughness due to J-integral remains between 110% and 140% for all mixes including 2.0 wt.%. On the other hand, the increase in critical energy release rate decrease with increasing the content. In fact, at 1.5 and 2.0 wt.% content the critical energy release rate decreases by 20% and 34% respectively. Nonetheless, COOH-MWCNTs prove more effective in improving the fracture toughness of PC than P-MWCNTs by achieving a maximum improvement of 112% at 0.5 wt.% COOH-MWCNTs content compared to 56% at similar P-MWCNTs content.

Both types of MWCNTs overall showed a decreased efficiency in improving the fracture toughness of PC with increasing their content. In fact, for both types of nanoparticles the highest improvement was reported at 0.5 wt.% content. ANPs on the other hand provided improved total fracture energy with increasing their content. The improvements continue from 45% in total fracture energy at 0.5 wt.% content up to 128% at 3.0 wt.% content. However, the mechanisms in which these improvements are achieved differ greatly. From 0.5 wt.% content up to 2.0 wt.%, the fracture energy from J-integral increase from 54% to 171% while the elastic energy drops down from 29% at 0.5 wt.% content to -14% at 2.0 wt.%. At 3.0 wt.% content however, the J-integral fracture energy increase is less effective as it drops from 171% at 2.0 wt.% to 113%. The elastic fracture energy however increases dramatically reaching an improvement of 155%.

Because of their extreme small dimensions, nanoparticles provide significantly large area at very low contents. By increasing their content, their polymer interactive abilities and mechanism differ greatly. Such abilities can be separated into chemical and mechanical in which they manipulate mechanical properties. In order to evaluate the overall effect of incorporating nanoparticles on improving the fracture toughness, the difference in these mechanisms can be ignored and their effectiveness can be evaluated with an overall total fracture energy parameter. With such parameter, it can be concluded that ANPs and COOH-MWCNTs both were able to provide a significant 128% and 112% increase in total fracture energy. Those improvements however were observed at the maximum content examined for ANPs of 3.0 wt.% content and the minimum COOH-MWCNTs content of 0.5 wt.%. P-MWCNTs still provided good improvements of 56% at 0.5 wt.% content as well. On the other hand, all nanoparticles

at all contents (with the exception of 1.0 wt.% content of P-MWCNTs) provided improvements in J-integral fracture energy. It can be assumed that J-integral fracture energy is generated by the nanoparticles mechanical properties. Thus, a general trend of either an increase in J-integral energy with the increase in content or a steady increase can be observed with between 0.5 wt.% and 1.5 wt.% for P-MWCNTs and COOH-MWCNTs and 0.5 and 2.0 wt.% for ANP. Increasing the content beyond these limits however result in a decrease from their previous maximum. This decrease can be correlated to a noticeable drop in flowability. Those changes are caused by the increased difficulty in obtaining dispersion which results in reduced viscosity and flowability. Chemical changes are described further using microstructural analysis and FTIR results.

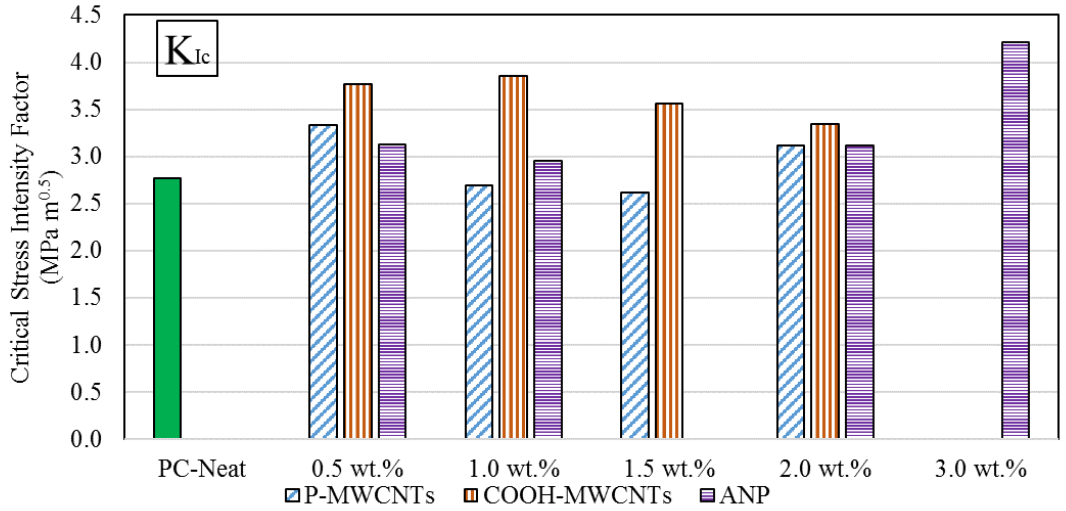

Figure 32: The critical stress intensity factor per QBFM analysis

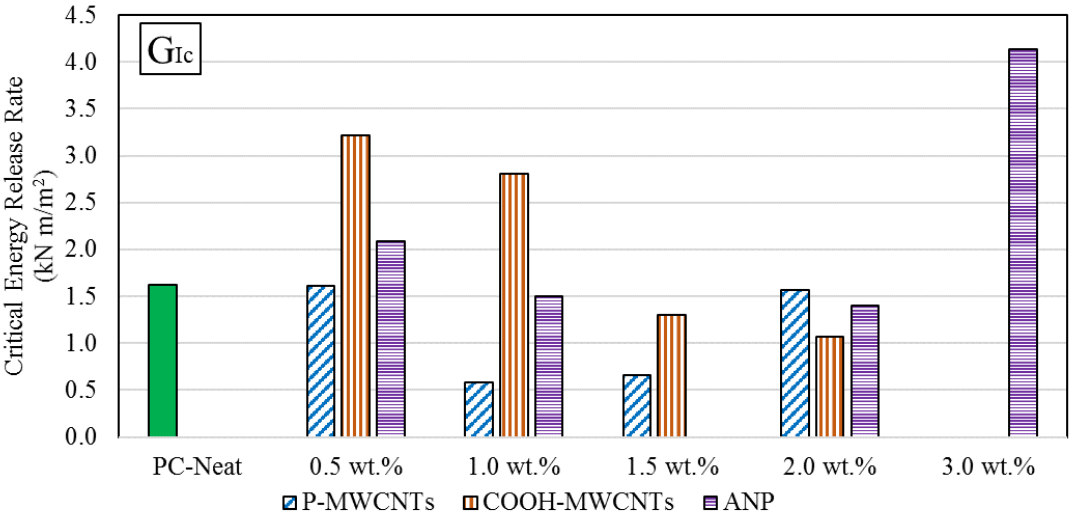

Figure 33: The critical energy release rate per QBFM analysis

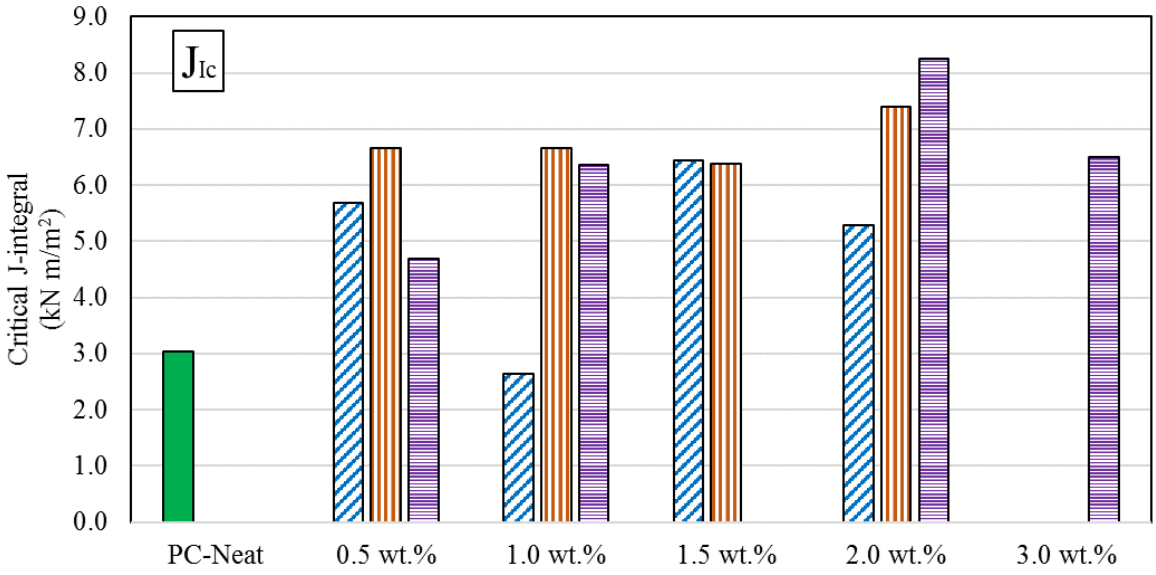

Figure 34: The critical J-integral values per QBFM analysis

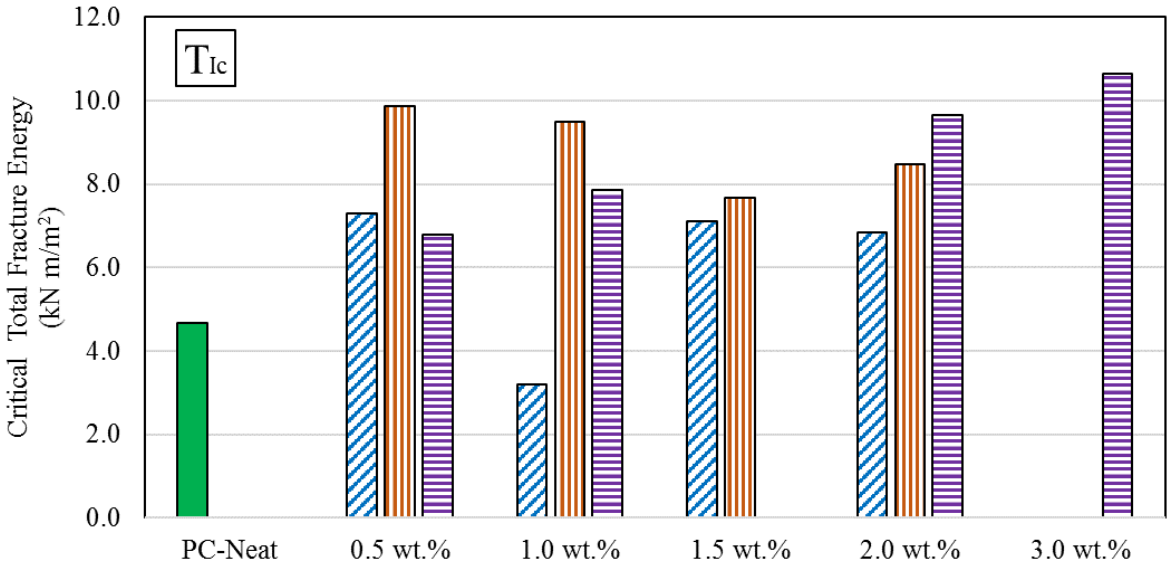

Figure 35: The critical total fracture energy per QBFM analysis

Finite element modeling of PC overlays with steel substrate

Finite element analysis was proposed to be developed to similar the behavior of PC overlay under flexural loading. In which, a representative volume element model to similar the behavior of PC under flexural stress and to also predict the change in PC electrical conductivity as a result of microcrack development. A snapshot from some preliminary finite element modeling by the PI of PC-steel deck overlay is shown in **Figure**

36. The finite element model developed in an ANSYS/ABAQUS environment and individual materials can be classified and the interface between layers can be described using interface elements. Results of flexural testing provided promising results and great improvements due to incorporating nanoparticles. Therefore, this section's focus was shifted towards only finite element modeling of the bond strength of PC with steel substrate which requires further investigation. Bond strength of PC to steel substrate is most suitably examined through slant shear testing. In those tests, PC is placed on top of a steel substrate sandblasted to a minimum of 4.0 mil (0.1016 mm) clean. The steel surface is inclined at 60° with the horizontal as shown in **figure 37**. Experimental tests were performed in order to evaluate the apparent shear strength as given in equation 20 as well as validate the finite element models.

$$\tau = \frac{P\sin(60)}{A/cos(60)} = \frac{P}{A}\sin(60)\,cos(60) \qquad (20)$$

Where P is vertical applied load and A is the cross-sectional area of the cylinder.

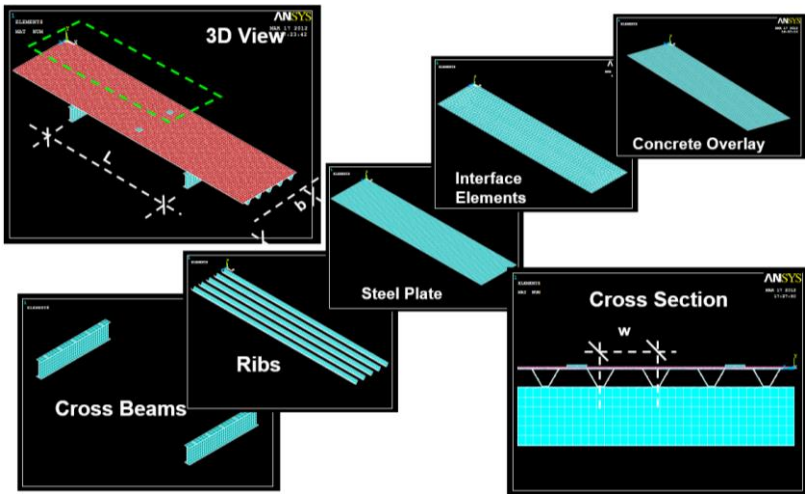

Figure 36: Preliminary finite element model of orthotropic bridge deck with PC overlay showing example model to be developed to determine the stress state in PC overlay.

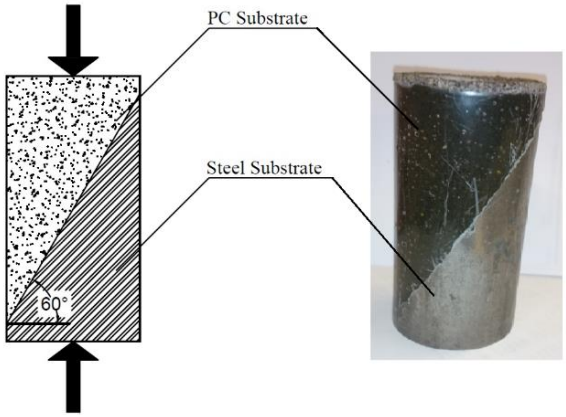

Figure 37: Slant shear test schematics and an actual specimen showing both substrates.

Finite element analysis of the slant shear test configuration was conducted using ABAQUS modeling software. PC was defined as a nonlinear elastic-plastic material using the constitutive stress-strain response measured in the uniaxial compression tests. The steel was assumed to be elastic perfectly plastic material. Convergence studies used two different types of built-in elements: 8-node linear hexagonal and 6-node linear triangular. These element types are capable of producing computationally inexpensive solutions for stress calculations. For each element type, different mesh sizes were used varying from 9,480 elements to 74,524 elements. Boundary conditions fixed the steel part from the bottom and prevented lateral deformation of the assembly. **Figure 38 (a)** shows the boundary conditions as applied on the model. **Figure 38 (c)** shows the meshed model using 6-node linear triangular elements. Displacement was applied to the top of PC to simulate slant shear tests. Load-displacement curves were extracted from the simulations and compared to those observed in the slant shear tests.

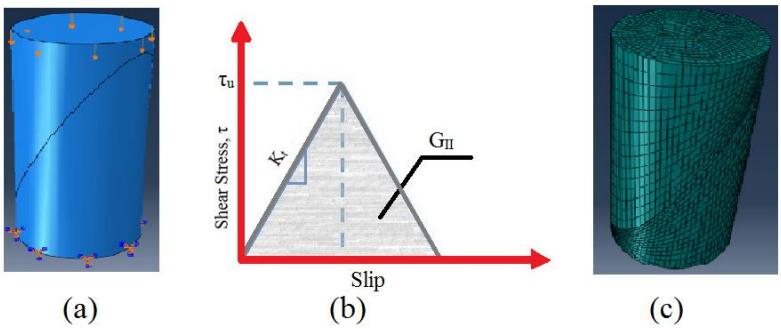

Figure 38: FE model using ABAQUS simulation environment: (a) Boundary conditions (b) Bilinear shear stress-slip relation where Kt is shear contact stiffness, GII is mode II fracture energy and τu is maximum shear stress (c) Meshed model using 74,524 elements.

In order to define contact between PC and steel, a zero-thickness cohesive contact element was defined. Bilinear shear stress-slippage relationship was used to describe the contact element as shown in **Figure 38 (b)** [67, 68]. This relationship is based on pure in-plane shear fracture mode (mode II) and is defined in ABAQUS using damage and cohesive behavior interaction [69]. The cohesive element characterizes the initial slope of the stress-slip curve (K_t) which is governed by the interfacial stiffness between the two slant shear test parts. The damage element on the other hand is prescribed using three components; initiation, evolution and stabilization. Firstly, damage initiation represents that maximum nominal stress in shear fracture mode (τ_u) characterized by the peak of the stress-slip curve. Secondly, damage evolution in this model was used based on the critical energy release rate in mode II (G_{II}) which denotes the area under the stress-slip curve. Finally, damage stabilization represents the energy dissipation module and is governed by the viscosity coefficient (V). In general, lower values of V signify rapid energy release and since failure in slant shear test is sudden, a constant low value of 0.001 was selected for all models. The values of τu, GII, V and Kt were determined through experimental validation of the FE simulation and back-solving for those parameters [70]. This was performed using a trial and error for-loop were the values of the cohesive and damage model were estimated and the resultant load-displacement curve of the simulation was matched with the experimental. Our objective is to use the validated FE model to realize the local shear stresses developed at failure of the slant shear test. Table 3 summarizes the contact interaction properties. **Figure 39** shows load-displacement curves for both FE model and slant shear test for the selected mixes namely PC-Neat, PCNC-0.5, PCNA-0.5, PCNA-2.0.

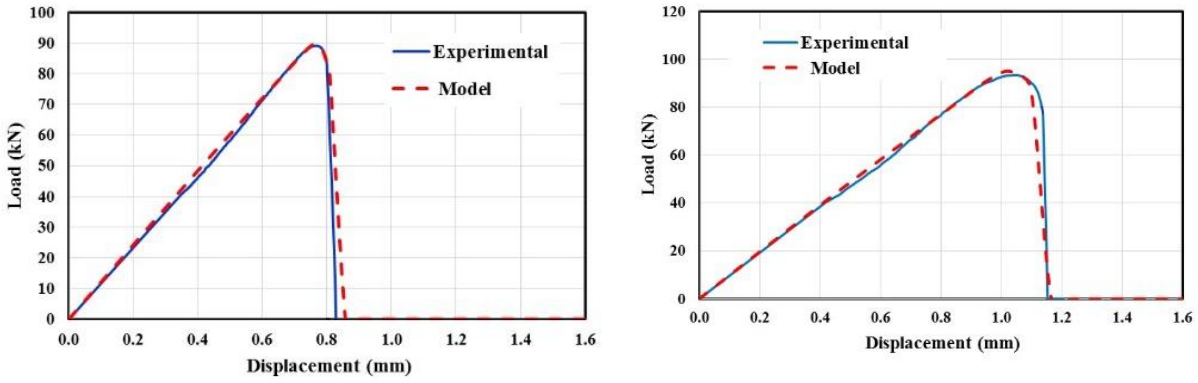

(a) (b)

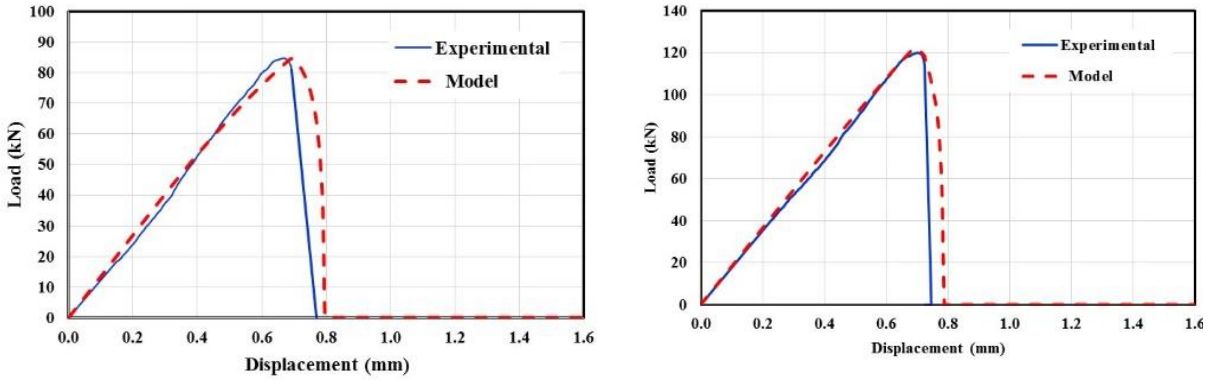

(c) (d)

Figure 39: Load-displacement curves of PC with different nanomaterials as measured experimentally during slant shear test and extracted using the finite element method for (a) PC-Neat, (b) PCNC-0.5, (c) PCNA-0.5, (d) PCNA-2.0.

Apparent shear/bond strength results of slant shear tests of PCN and steel are shown in **Figure 40**. All test specimens failed at the adhesion interface and no cohesive failure was observed as shown in **Figure 41**. As explained later interpreting the results of FEA, the samples failed when the fracture energy criteria G_{II} was reached. Hence, sudden failure was observed in the mechanical testing of slant shear where as FEA explored the critical location over the shear interface where the fracture criteria was satisfied. PCNs showed a significant increase in apparent bond strength compared with neat PC. Results of mixes incorporating COOH-MWCNTs at 0.5, 1.0 and 2.0 wt.% showed a similar increase of 7% in apparent bond strength compared with neat PC. This result suggests no advantage with respect to apparent bond strength by using COOH-MWCNTs beyond 0.5 wt.%. An increase in ANPs content corresponded to increase in apparent bond strength: apparent bond strengths of 20, 23 and 51% above neat PC with 0.5, 1.0 and 2.0 wt.% of added ANPs, respectively. This result may be attributed to the possible chemical reactions of ANPs with -OH groups formed on sand blasted steel surface leading to higher bond strength.

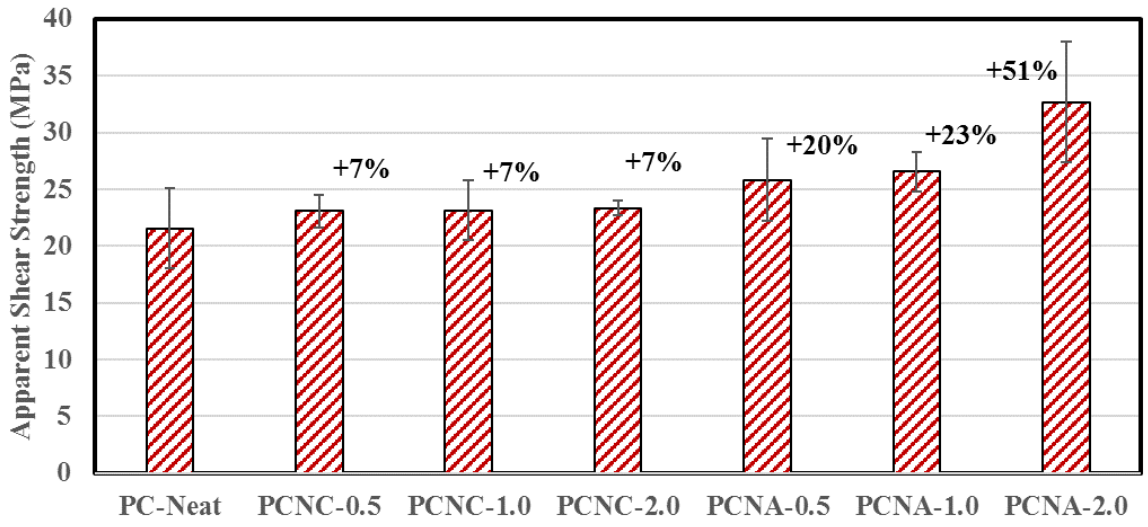

Figure 40: Apparent shear strength of all PC mixes (MPa)

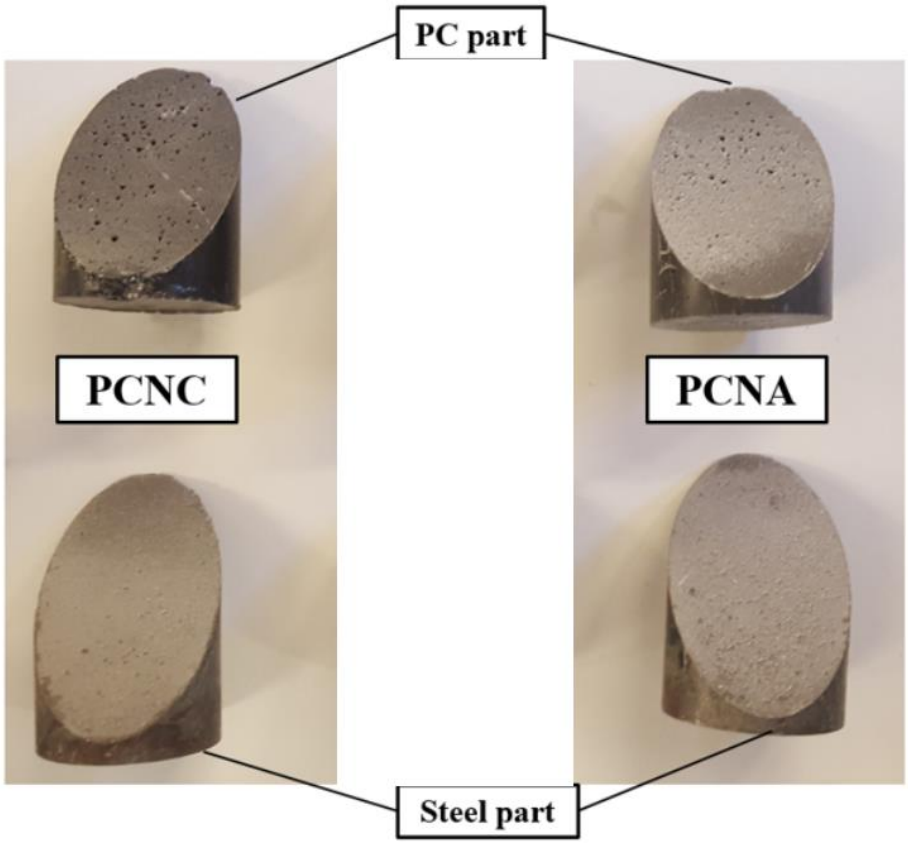

Figure 41: Slant shear fracture surface post-failure for all PC mixes showing complete adhesion failure.

Finite element analysis results of shear stress are shown in **Figure 42** and were also used to examine the interfacial shear stress contours at the PC-steel interface. **Figure 43** shows the load-displacement of neat PC extracted from the FE model with magnified slippage in the assembly at vertical displacements of 0.720 mm, 0.802 mm, and 0.837 mm. At each of these points, shear contours on the interface were plotted showing the maximum local shear stress to reach 40 MPa. Locations of maximum local shear stress concentration on the interface are shown in **Figure 43**. Maximum local shear stress only develops at the location of minimum height of PC before reaching ultimate load as shown in **Figure 43** and **Figure 44 (a)**. As slippage occurs, the maximum local shear stress moves along the interface. The maximum local shear stress path follows the height of PC from minimum to maximum as shown in transition in **Figure 44** from **(a), (b)** and **(c)**. Slant shear tests show that complete slippage occurs after the ultimate load due to release of energy as a result of bond failure.

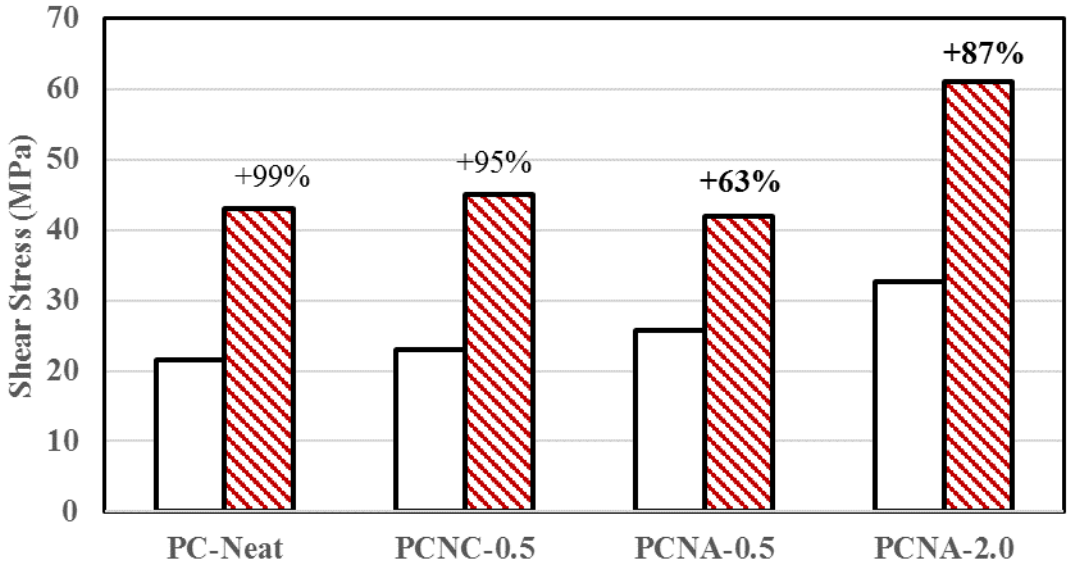

Figure 42: Shear strength for different PC incorporating nanomaterials interpreted using apparent shear strength (average stress based on slant shear standard) and maximum local shear stress using the finite element model. The % difference shown is the difference

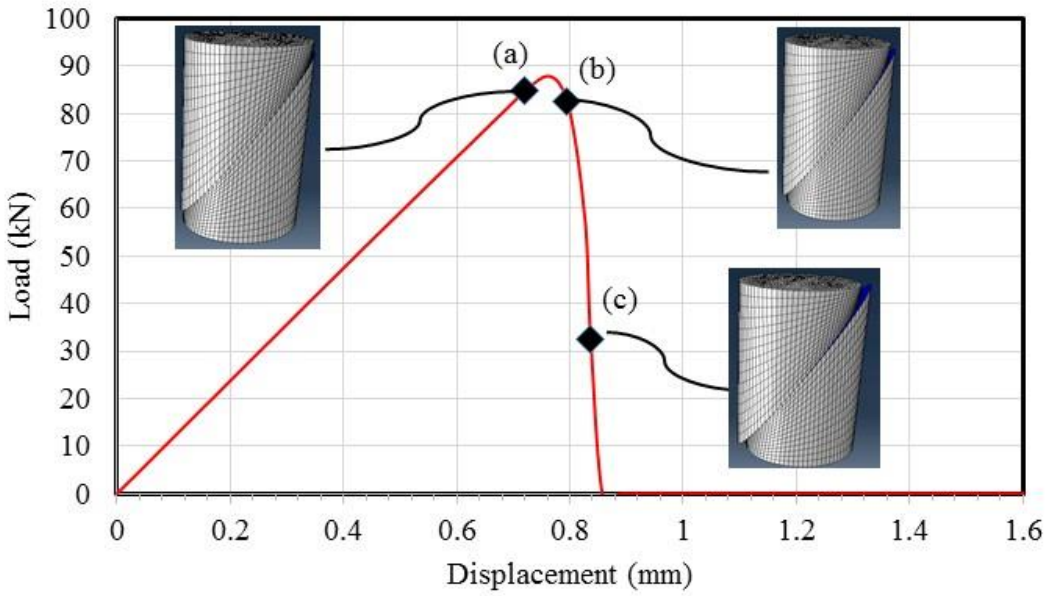

Figure 43: Load-displacement extract from finite element analysis of neat PC showing magnified slippage at 0.720mm, 0.802mm, and 0.837mm.

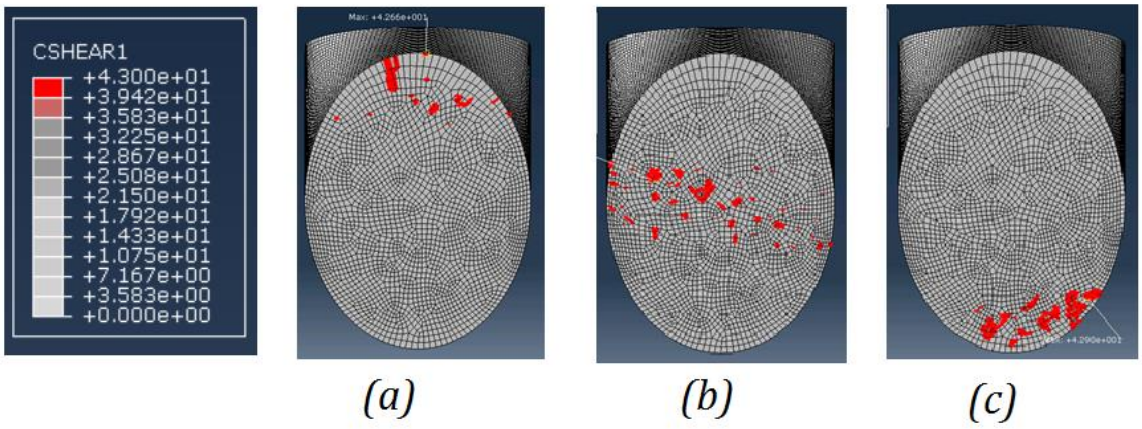

Figure 44: Shear contours showing locations of maximum local shear stress during slippage at vertical slip of (a) 0.720 mm (b) 0.802 mm and (c) 0.837 mm

Microstructural Analysis

Microstructural analysis consisted of Scanning electron microscope (SEM) as well as Fourier Transform Infrared Spectroscopy (FTIR). SEM were designated to examine the effectiveness of dispersion of all nanoparticles at different contents. The device used is Hitachi S-5200 Nano SEM which is capable of magnification within the range of 100-2

million with a resolution of 1.7 nm at 1 kV and 0.5 nm at 30kV. Due to the polymeric nature of the epoxy, charging hindered the use of high voltage measurement and all scans were collected at 2.0 and 5.0 kV. In order to better understand the chemically induced effects, FTIR scans were acquired for all nanoparticles at different contents. Scans were acquired using a horizontal Attenuated Total Reflectance (ATR) and a DiComp Crystal made of a diamond ATR with Zinc Selenide focusing element were used to collect 4000 scans at a resolution of 4 cm^{-1}. The samples were of 25.4 cm^2 and 2 mm thickness of similar mixes to those discussed in DMA and SEM. Analysis of scans were performed using PerkinElmer FTIR with Universal ATR (UATR) accessory. The scans were converted to absorbance using Kramers-Kronig equations [71].

SEM scans are collected for 0.5 and 2.0 wt.% content of P-MWCNTs and COOH-MWCNTs as shown in **figure 45** and **46** and 0.5 and 3.0 wt.% content of ANPs as shown in **figure 47**. Scans of neat samples were also collected as reference for all scans as shown in **figure 48**. Those scans provide both extremes of the contents examined during mechanical testing. All previous scans show that sufficient nanoparticles dispersion is achieved using the described dispersion technique. Scans with P-MWCNTs further examined the networking abilities of those particles that enable electrical conductivity described earlier in fatigue and SHM. Those networks however didn't appear in scans of 0.5 wt.% content and only were noticeable at 2.0 wt.% confirming percolation limit. Those networks aid in increasing the resistivity of PC samples up to measurable levels that can aid in quantifying mechanical damage. COOH-MWCNTs chemically interact with polymeric chains and hence don't develop such network as those observed with P-MWCNTs. ANPs are similar to P-MWCNTs as they don't interact with the polymer matrix. However, unlike MWCNTs, ANPs are of a smaller dimension and their scans can only show embedment of the nanoparticles into the epoxy polymer matrix.

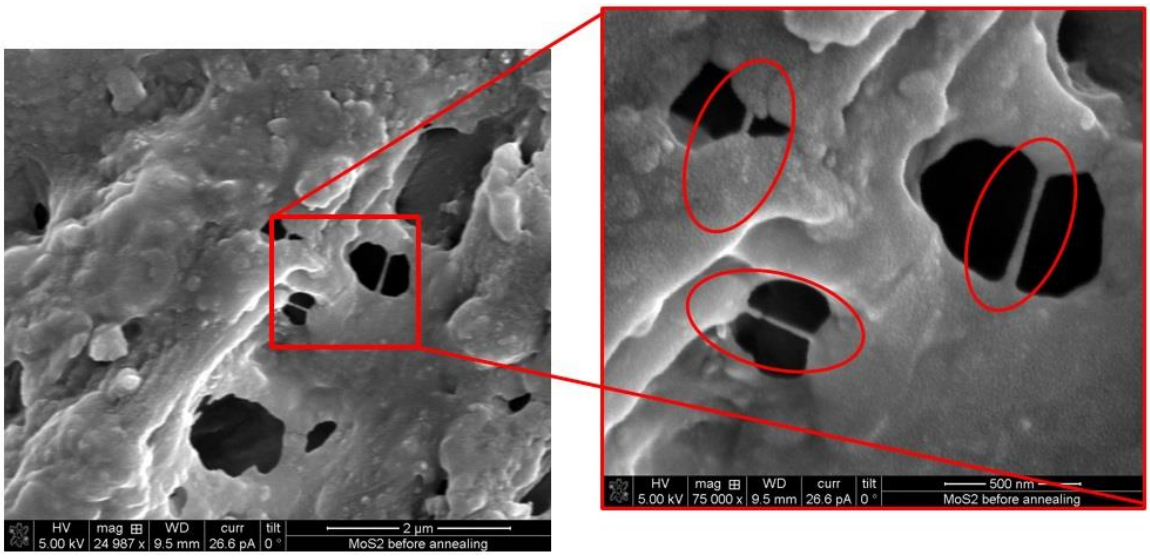

(a)

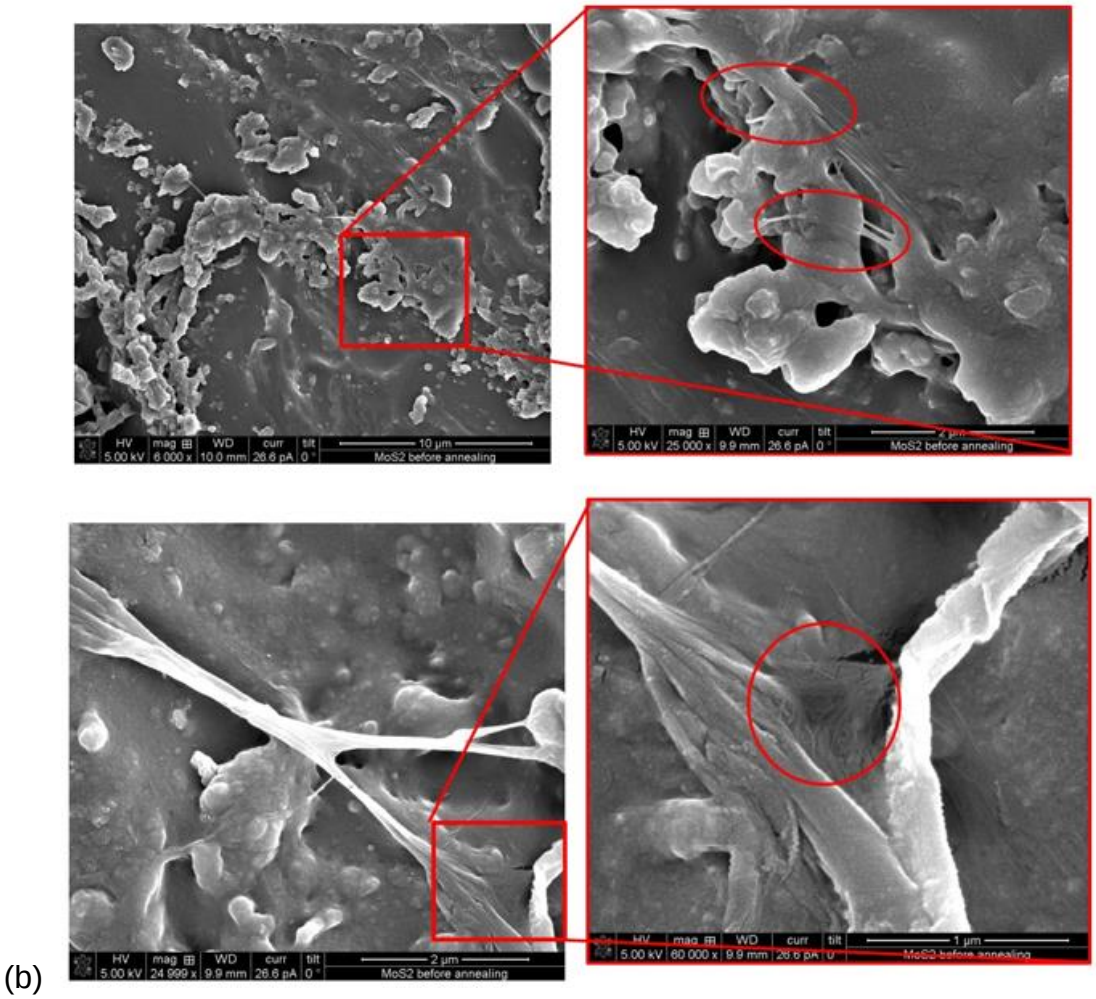

(b)

Figure 45: SEM scans for hardened epoxy containing (a) 0.5 wt.% content P-MWCNTs and (b) 2.0 wt.% content P-MWCNTs.

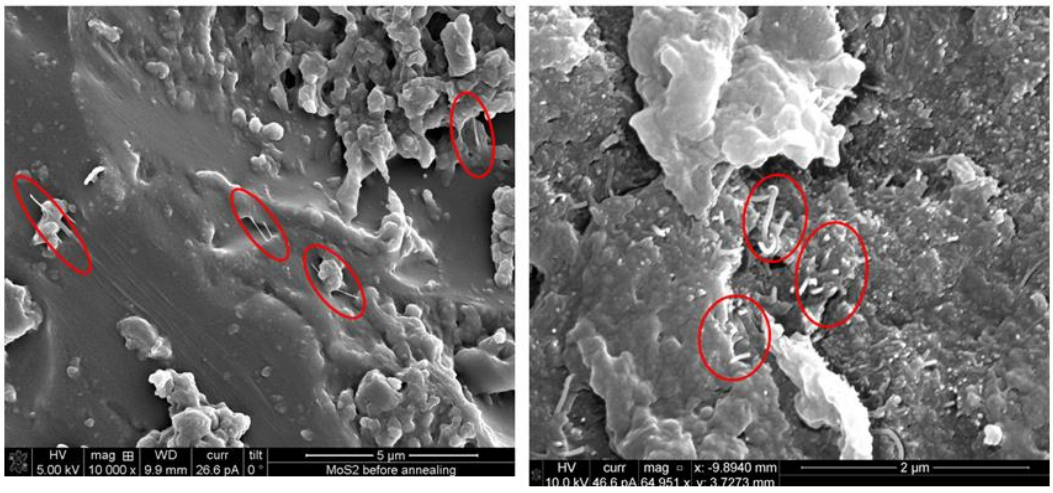

Figure 46: SEM scans for hardened epoxy containing 0.5 wt.% COOH-MWCNTs (left) and 2.0 wt.% COOH-MWCNTs (right).

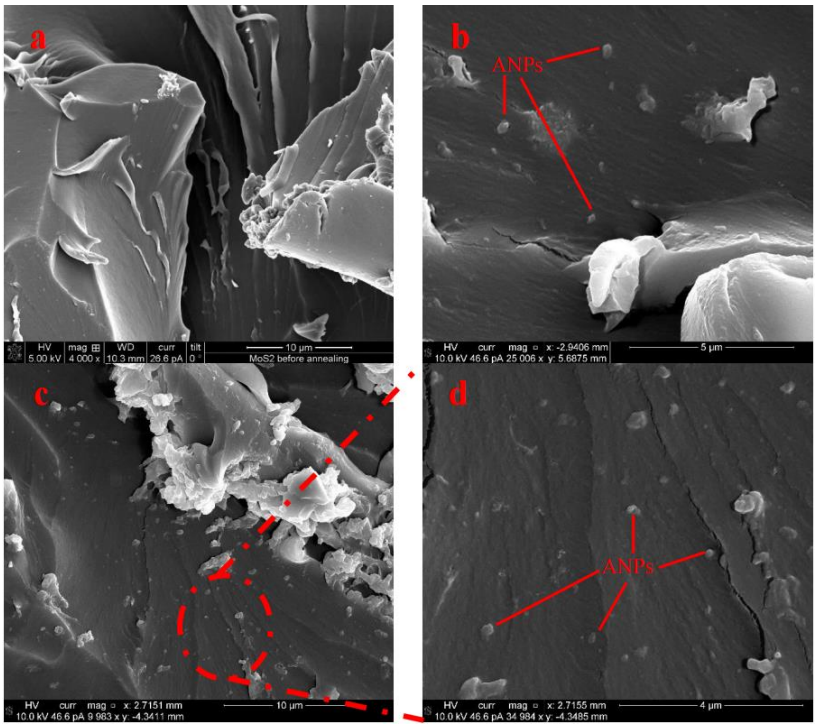

Figure 47: SEM scans for hardened epoxy containing (a) and (b) 0.5 wt.% ANPs and (c) and (d) 3.0 wt.% ANPs.

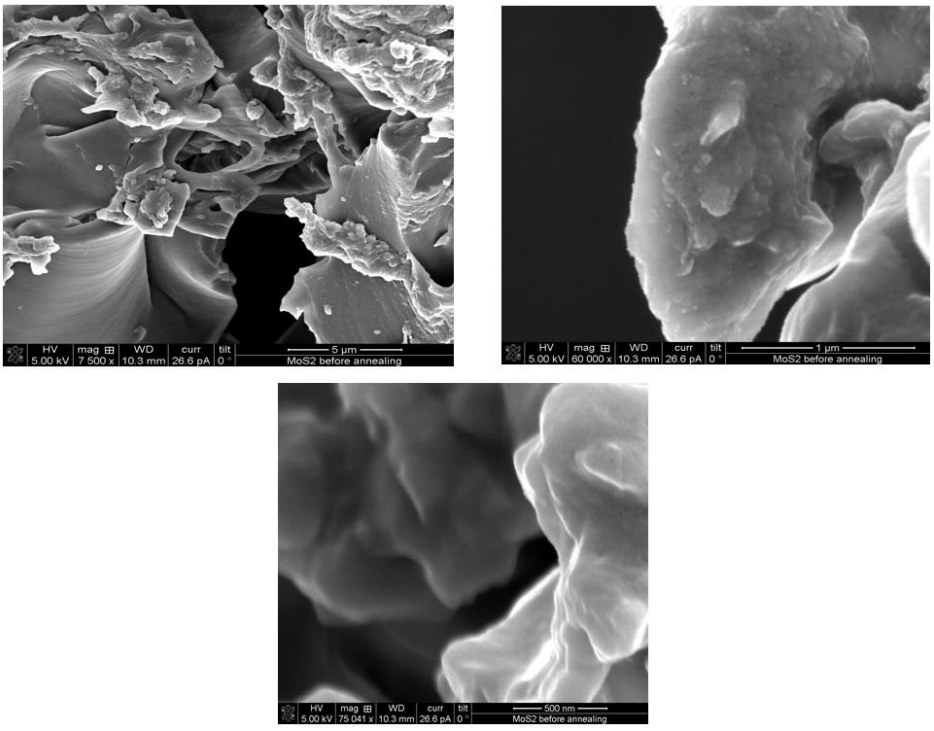

Figure 48: SEM scans for neat hardened epoxy.

FTIR spectrographs of neat epoxy and epoxy with 0.5 and 2.0 wt. % of P-MWCNTs are shown in **Figure 49**. The characteristic peaks of the synthesized siloxane-epoxy/P-MWCNTs samples appeared at 3330–3500 cm−1 (O-H), 2750–2940 cm−1 (C-H), 1460 cm−1 (C-H, CH2 and CH3), 1039–1100 cm−1 (Si-O-Si and C-O-C), 1250–828 cm−1 (C-H in Si-CH3), 560 cm−1 (Si-O-Si) [17-19]. A peak appears near 1605 cm−1 due to Si–C6H5 vibrations [23]. The remaining epoxy groups (oxirane ring) appeared at 940 cm−1. The spectrographs of the three MWCNTs show no different and thus do not indicate any chemical interaction with P-MWCNTs because non-functionalized MWCNTs was used in the preparation of the PC composite. The ability of the relatively low content of P-MWCNTs (0.5 wt. %) to alter the mechanical properties might be attributed to the interaction between the nanoscale MWCNTs and epoxy. FTIR peaks in the spectrographs show that the peaks of the epoxy compounds in epoxy incorporating 0.5 wt. % P-MWCNTs is higher than that of the neat epoxy. More interestingly, FTIR peaks of epoxy incorporating 2.0 wt.% P-MWCNTs is lower than that of neat epoxy. The above observation can be explained by considering the ability of nanotubes to hinder epoxy reaction. At a low P-MWCNTs content < 0.5 wt.%, it seems that MWCNTs inhibit epoxy reaction resulting in lower cross-linking than that of neat epoxy. This in its turn results in reducing PC strength and improving PC strain at failure and fracture toughness.

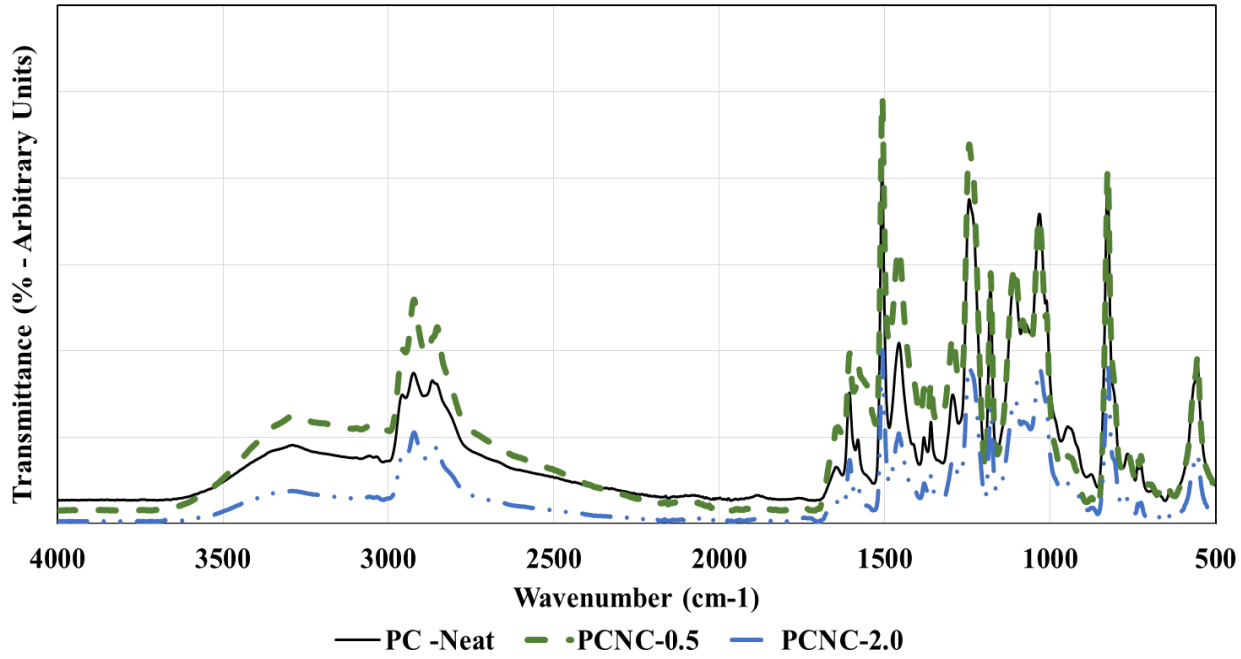

Figure 49: Results of neat PC, 0.5 and 2.0 wt.% MWCNTs FTIR spectrograph

On the other hand, increasing the P-MWCNTs content gradually results in reducing that effect of inhibiting epoxy reaction. That might be to the fact that MWCNTs will tend to agglomerate and entrap air which would reduce the strength. However, the relatively

large MWCNTs content helps in maintaining the integrity of PC and allows it to slightly improve the strength and strain at failure. It is apparent that the significance of MWCNTs on strength and fracture can be explained based on its chemical effect at relatively low content< 0.5 wt.% but the explanation becomes extremely complex with many interdependent factors at high P-MWCNTs content. Further research is warranted to measure the cross-linking density of epoxy incorporating the different amount of MWCNTs.

To compare the effect of functionalization of MWCNTs with carboxyl groups (COOH), scans of samples containing 0.5 wt.% of both P-MWCNTs and COOH-MWCNTs were examined. **Figure 50** shows the respective spectrograph. With COOH-MWCNTs, a new band appears at 1750 cm^{-1}. This new band is attributed to the C=O stretching which is due to the ester group being formed as a result of the esterification reaction between the epoxy resin and the carboxylic group of the functionalized COOH0MWCNTs as reported by Zou et al. [72] and Kim et al. [73]. This reaction, specifically at higher MWCNTs content, will result in increasing epoxy crosslinking and thus creating a stiffer and stronger PCNC compared with PC-Neat.

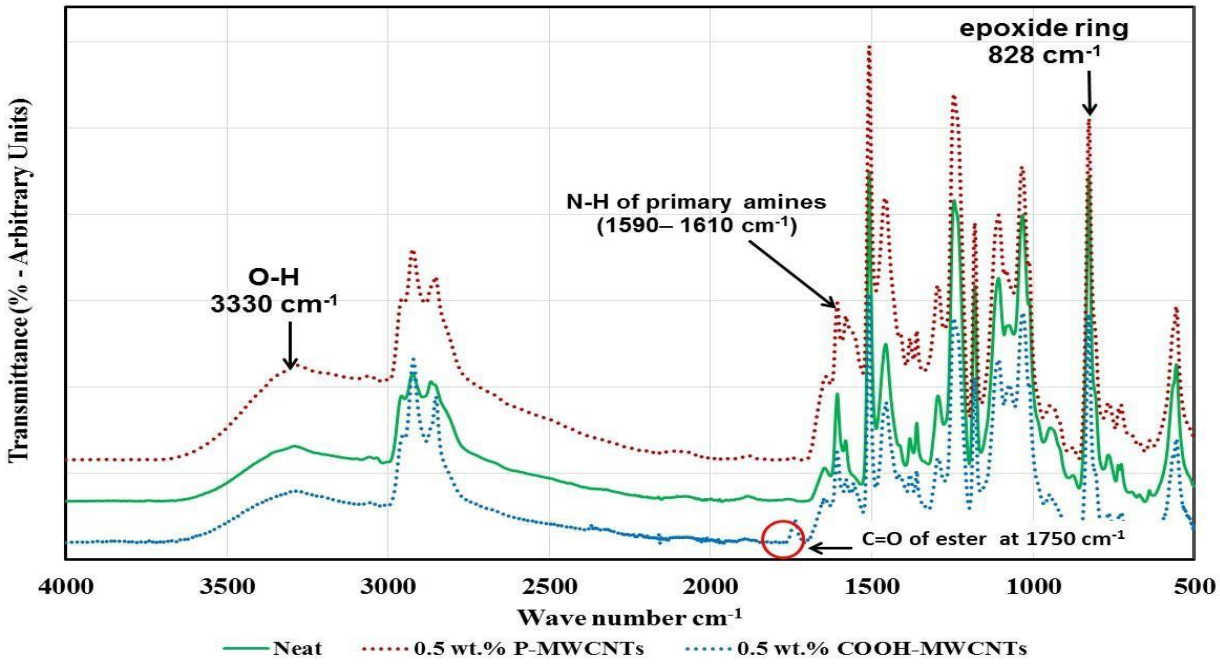

Figure 50: Results of PC-Neat and 0.5 wt.% P-MWCNTs and COOH-MWCNTs FTIR spectrograph

Comparing the O-H stretching bands of all epoxy-ANPs nanocomposite spectra with that in the neat specimen shown in **figure 51**, it is noticed that O-H bands of epoxy-ANPs nanocomposites show lower absorption height with broader bands than that of the neat epoxy sample. This observation might be attributed to the effect of ANPs on the O-H 13 association. It is well known that the broad complex band of the hydroxyl stretching vibration region at about 3200–3600 cm−1 is attributed to the combined effect of the differently associated hydroxyl groups, i.e. hydrogen bonding between hydroxyl and hydroxyl/carbonyl groups of different strength and hydrogen bonding of water molecules. In addition, a matrix having O–H groups could undergo two modes of hydrogen bonding: inter- and intramolecular hydrogen bonds between O–H groups [74]. Overall, the O–H band broadening and intensity lowering can be attributed to redistribution in the arrangement of the hydroxyl group association due to the different geometry caused by the lowered cross-linked matrix. Consequently, the authors hypothesize that incorporating ANPs in the epoxy matrix reduced 295 epoxy crosslinking. Lowering the crosslinking bonds consequently changed the ratios of hydrogen bonding modes, which lead to different geometry with different force constants and consequently broadened O-H bands with lower absorption values as those observed in **Figure 51**. The above microstructural analysis explains the ability of ANPs to produce PC with appreciable strength, superior ductility and improved fracture toughness. The ability of ANPs to reduce epoxy matrix crosslinking intensity enables producing PC with significantly higher ductility than that observed by neat epoxy PC.

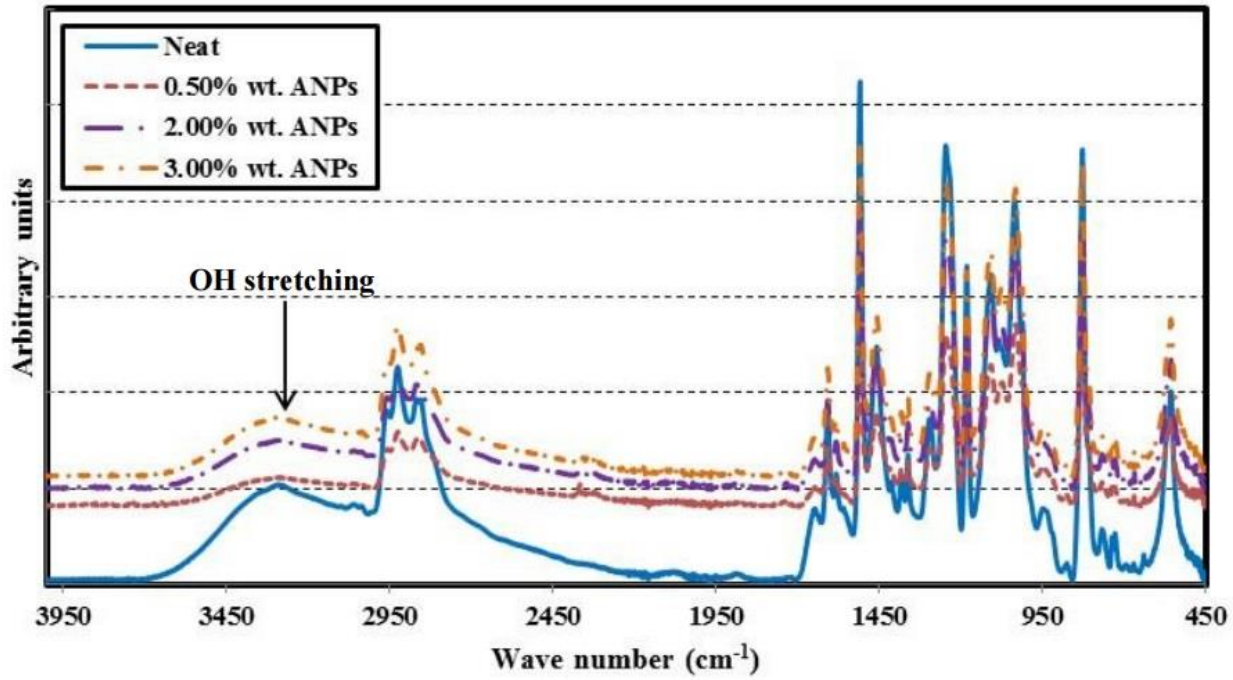

Figure 51: Results of PC-Neat and 0.5, 2.0 and 3.0 wt.% ANPs FTIR spectrograph

Field implementation of PC incorporating nanomaterials

In this task, one mixtures of PC incorporating 3.0 wt.% P-MWCNTs was down-selected from the top list of PC mixtures discussed in Stage 1. The field implementation was located at University of New Mexico (UNM) campus in Albuquerque, New Mexico. The selected site is a concrete slab used as a parking area and designed to resist truck loads. The area is also exposed to normal service conditions including freeze-thaw, wetting and drying and combined thermal and humidity conditions. Two top cover of 1.0 in (25 mm) 1.5 in (38 mm) of the existing slab were stripped off to produce two samples with different thickness. The existing concrete surface was prepared to standard roughness as per ACI guidelines [4]. Copper electrodes were embedded in the PC during placement to enable later connection to electrical conductivity measurements during field testing.

The two PC overlays were cast beside each other with each strip being 12-inch (300 mm) width and 16 in (400) long separated from each other by a spacing of 8 ft (2.5 m). A total of two strips including two PC with P-MWCNTs. The detailed process in making the PC samples with nanomaterials is described in **Figure 52**. The field samples were heat cured at 65°C for 48 hours to ensure the polymerization and establish the conductivity of PC. However, it is important to note that such heat curing is not necessary as PC will reach such level of polymerization and conductivity after 14 days of cast. The PC strips were left to be exposed to natural weather and cycles of wetting and drying at that field location for a time period of 12 months prior to field measurements.

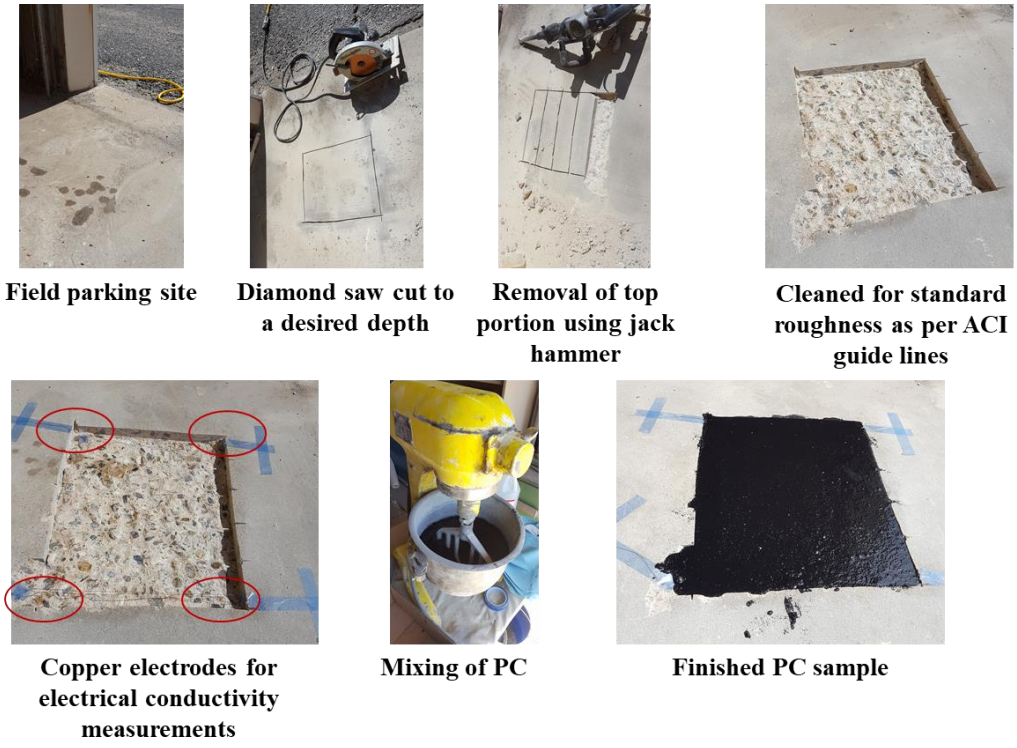

Figure 52: Procedure for field preparation of PC field samples.

Figure 53: Two PC field samples after one year of weather exposure.

The two PC field samples after being subjected to weather exposure in Albuquerque for 12 months are presented in **Figure 53.** The dimensions of sample P1 is 12 in wide, 16 in long and 1 in thick and sample P2 is 12in wide, 16 in long and 1.5 in thickness. Copper electrodes that were previously placed inside the PC samples were connected to a Keithley 2612B source meter to measure the electrical conductivity/resistivity of the PC field sample before and after loading. A Ford F-150 pickup truck was used to load the two field samples as shown **Figure 54**. Both field samples P1 and P2 were loaded using the wheel load three times. Electrical resistivity measurements were recorded before and after loading. Electrical resistivity measurements are presented in **Table 3**.

Table 3: Electrical resistivity measurements of field samples before and after loading

ID*	Reading #	Electrical resistance ($M\Omega$)	
		Before Loading	After Loading
P1	1	1.64	1.63
	2	1.61	1.59
	3	1.61	1.59
P2	1	15.15	14.98
	2	14.86	14.83
	3	14.76	14.68

The measurements in Table 3 shows that both field samples are conductive and electrical measurements can be performed in the field. It is important to note that regular PC is non-conductive, and its electrical resistance will be orders of magnitude higher than what was measured here. The difference in electrical resistance of P1 and P2 is attributed to thickness difference. It is also noted that there is negligible change in the electrical resistivity of the material before and after loading. This can be attributed to the limited stress caused by the loading truck and the fact that no cracking occurs in the PC field sample during loading. The premise is if cracking to take place, electrical conductivity measurements would change significantly. A detailed loading procedure with readings for both P1 and P2 field specimens is shown in **Figure 55** and **Figure 56**.

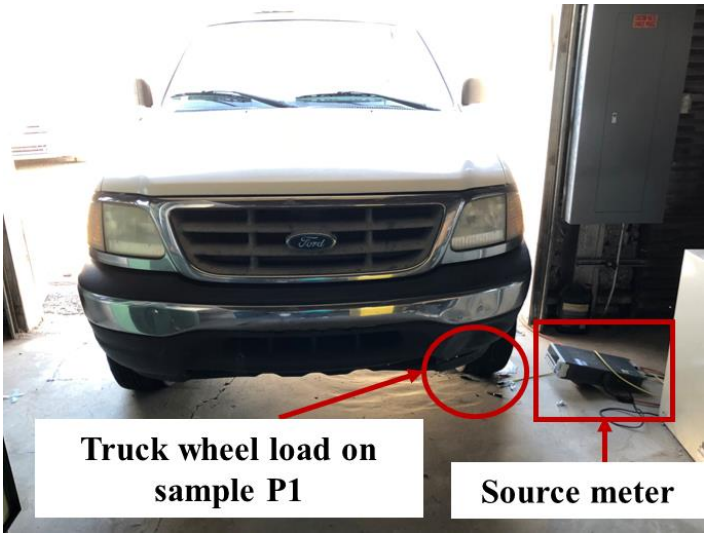

Figure 54: Ford F-150 truck wheel loading on the sample and conductivity measurements collected using source meter

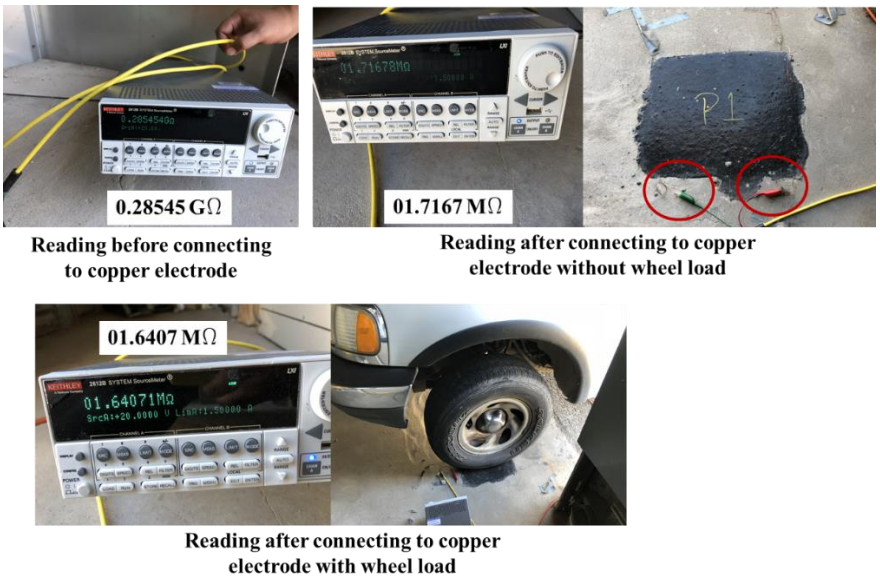

Figure 55: Electrical resistivity reading while loading the sample P1

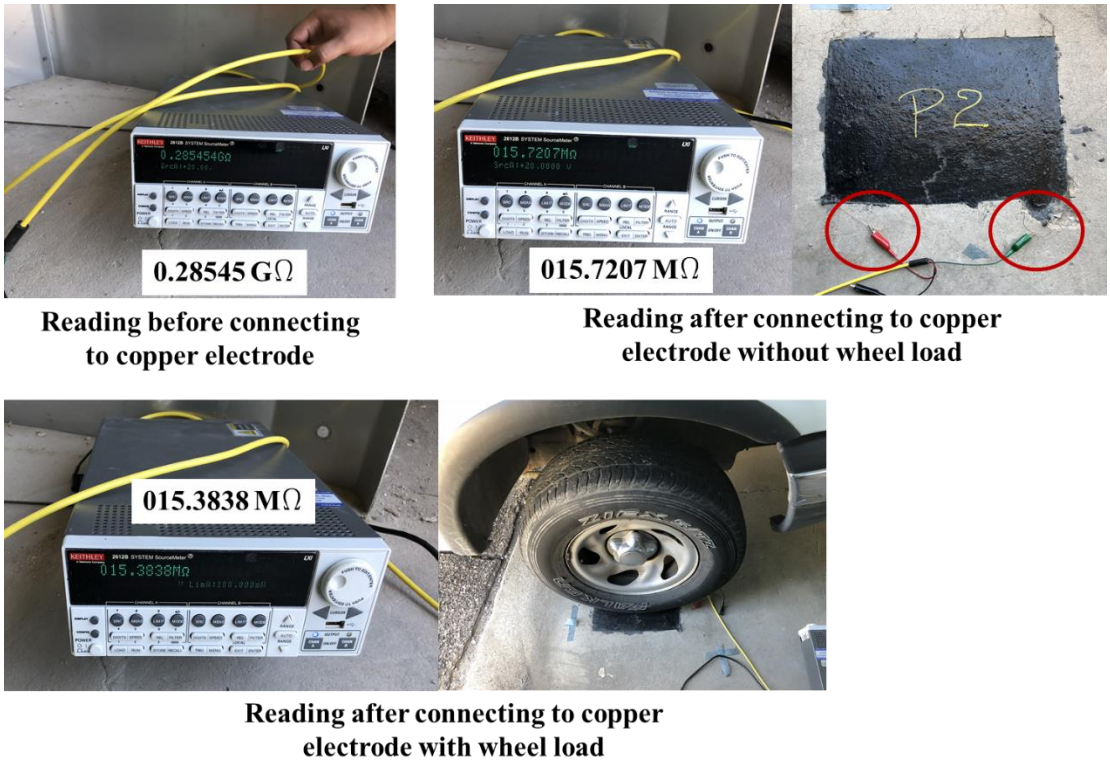

Figure 56: Electrical resistivity reading while loading the sample P2

The above results clearly indicate that the PC with nanomaterials can be used in the field and will enable the proposed self-sensing. After 12 month of field and weather exposures including wetting, drying and temperature cycles, the PC field samples were conductive and were able to provide a proof for the material ability to perform expected functionality in the field.

CONCLUSIONS

The above experimental investigations show that it is possible to improve the bond strength, ductility, fracture toughness and fatigue performances of PC using nanomaterials such as multi-walled carbon nanotubes (MWCNTs), or alumina nanoparticles (ANPs). Incorporating P-MWCNTs resulted in small decrease in tensile strength with a minimum appreciable tensile strength of 9 MPa. The strain at failure, however, increased to 3.2%. COOH-MWCNTs results show a different behavior by increasing the tensile strength up to a maximum of 15.4 MPa with a decrease in strain at failure to 0.8%. ANPs showed similar results to that of P-MWCNTs with a minimum of 9.5 MPa and an improved tensile strain at failure of 4.9%. Thus, incorporating nanoparticles resulted in a maximum decrease of tensile strength by 22% countered by a maximum improvement in strain at failure by 91%. The significant improvements achieved were clearly reflected with improvements in PC's toughness by a maximum of 80%, and 135% for P-MWCNTs and ANPs respectively.

P-MWCNTs were solely investigated for fatigue performance as COOH-MWCNTs bond with the host polymer matrix and ANPs do not provide a conductive network. Fatigue performance of P-MWCNTs PC mixes showed improvements in fatigue life up to 1240% at 2.0 wt.% content. PC samples in all mechanical tests exhibited non-linear behavior redeeming linear elastic fracture mechanics (LEFM) analysis, often used for concrete, invalid. Quasi-brittle fracture mechanics (QBFM) was therefore used for the analysis of the fracture toughness parameters of PC with nanoparticles. PC incorporating P-MWCNTs, COOH-MWCNTs and ANPs improve the total fracture toughness by 52%, 112%, and 128% respectively. Improvements with P-MWCNTs mixes were achieved mainly with plastic fracture toughness while ANPs and COOH-MWCNTs achieved improvements in both elastic and plastic fracture toughness. PC with nanoparticles provided strong bond to steel substrates with improvement in bond strength up to 51%. Self-sensing of PC incorporating P-MWCNTs using electrical conductivity/resistance measurements is possible. The percolation level of P-MWCNTs is achieved at such low content (about 2%) allowing mechanical damage to be correlated to the change in electrical resistance.

SEM images of all epoxy nanocomposite reveal that uniform dispersion was achieved using shear mixing and ultrasonication. FTIR spectrographs reveal that both P-MWCNTs and ANPs delay the epoxy polymerization and thus reduce PC crosslinking density thus improve ductility. On the other hand, COOH-MWCNTs react with the host epoxy matrix forming C=O ester bonds that increase the level of crosslinking density and improve strength.

Finally, field implementation of PC with P-MWCNTs was executed on two field specimens. The field two specimens were produced in a parking area at UNM campus. The two field specimens were left to typical traffic and weather exposures including thermal cycles and wetting and drying conditions for 12 month prior to field testing. Field test under truck loads showed the two specimens to be electrically conductive and to enable measurements during loading.

It is evident from the above investigation that PC incorporating nanoparticles provide a promising material that can be engineered for improved mechanical enhancements in bond strength, ductility, fatigue life and fracture toughness. PC incorporating nanoparticles also has self-sensing capabilities. The proposed nanomaterials can be used to improve performance and prolonging service life of PC overlays.

REFERENCES

[1] ACI Committee 548, Polymers and Adhesives in Concrete, State of the Art Report, 2009.

[2] Kraus, P.D. Bridge Deck Repair Using Polymers, International Congress on Polymers in Concrete, North American Workshop, San Francisco, CA, USA, 1991.

[3] Koblischek, P.J. Polymer concrete as an alternative material for grey cast iron and steel weldments on machine tool applications, in: Proceedings of ICPIC, San Francisco, CA, USA, 1991.

[4] Abdel-Fattah, H. El-Hawary, M.M. Flexural behavior of polymer concrete, Constr. Build Mater. 13(5), (1999) 253-262.

[5] Hsu, H.T. Fowler, D.W. Creep and fatigue of polymer concrete, Polymer Concrete: Uses, Materials, and Properties, American Concrete Institute (ACI) SP-89, MI, 1985, pp. 323-341.

[6] Czarnecki, L. Chmielewska, B. The influence of coupling agent on the properties of vinylester mortar, in: Proceedings of the Second International RILEM Symposium on Adhesion between Polymers and Concrete, RILEM, Cachan, France, Sept. 1999, pp. 57-65.

[7] Heidari-Rarani, M. Aliha, M.R.M. Shokrieh, M.M. Ayatollahi, M.R. Mechanical durability of an optimized polymer concrete under various thermal cyclic loadings – an experimental study, Construction and Bldg. Mater.. 64 (2014) 308-315.

[8] Bedi, R. Chandra, R. Singh, S.P. Mechanical properties of polymer concrete, J. of Composites. Article ID 948745 (2013) 12 pages.

[9] Jo, B.-W., Park S.K, Park J.C., “Mechanical properties of polymer concrete made with recycled PET and recycled concrete aggregates”, Construction and Building Materials V. 22 (2008), 2281–2291.

[10] Shokrieh, M. M., Kefayati, A. R., Chitsazzadeh, M., “Fabrication and mechanical properties of clay/epoxy nanocomposite and its polymer concrete”, Materials and Design V. 40 (2012), 443–452.

[11] Li, Z., Wang, H., He, S., Lu, Y., and Wang, M. (2006). “Investigations on the preparation and mechanical properties of the nano-alumina reinforced cement composite.” Mater. Lett., 60(3), 356–359.

[12] Campillo, I., Guerrero, A., Dolado, J. S., Porro, A., Ibáñez, J. A., and Goñi, S. (2007). “Improvement of initial mechanical strength by nanoalumina in belite cements.” Mater. Lett., 61(8–9), 1889–1892.

[13] Hosseini, P., Hosseinpourpia, R., Pajum, A., Khodavirdi, M. M., Izadi, H., and Vaezi, A. (2014). “Effect of nano-particles and aminosilane interaction on the performances of cement-based composites: An experimental study.” Constr. Bldg. Mater., 66, 113–124.

[14] Soliman, E., Kandil, U. F., Reda Taha, M.M. “The Significance of Carbon Nanotubes on Styrene Butadiene Rubber (SBR) and SBR Modified Mortar”, Materials and Structures, V. 45, No. 6 (2012), 803–816.

[15] Sharmaa, R., and Iqbal, Z., “In situ observations of carbon nanotube formation using environmental transmission electron microscopy”, Applied Physics Letters, V. 84, No. 6 (2004).

[16] Ting, J. H., Lyu, J. Y., Huang, F. Y., Li, T. L., Hsu, C. L., Liu, C. W., “Synthesis of single-wall carbon nanotubes by atmospheric thermal CVD”, 17th Biennial

University/Government/Industry Micro-Nano Symposium - Proceedings, UGIM (2008), 157–160.

[17] Kim, J.A., Seong, D.G., Kang, T.J., and Youn, J.R. “Effects of surface modification on rheological and mechanical properties of CNT/epoxy composites,”, Carbon, V. 44, No. 10 (2006), 1898–1905.

[18] Vaisman, L., Wagner, H.D. and Marom, G. “The role of surfactants in dispersion of carbon nanotubes”, Advanced Colloid Interface Science, V. 128 (2006), 37–46.

[19] Kao, J. H. Polymer Nanocomposites: Processing, Characterization and Applications, McGraw-Gill Nanoscience and Technology Series, (2006).

[20] Seyhan, A.T., Tanoglu, M. and Schulte, K. “Mode I and mode II fracture toughness of E-glass non-crimp fabric/carbon nanotube (CNT) modified polymer based composites”, Engineering Fracture Mechanics, V. 75, No. 18 (2008), 5151–5162.

[21] Swain, S., Sharma, R. A., Patil, S., Bhattacharya, S., Gadiyaram, S. P., and Chaudhari, L., “Effect of Allyl Modified/Silane Modified Multiwalled Carbon Nano Tubes on the Electrical Properties of Unsaturated Polyester Resin Composites”, Transactions on Electrical and Electronic Materials, V. 13, No. 6 (2012), 267–272.

[22] Geng, Y., Liu, M.Y., Li, J., Shi, X.M. and Kim, JK. “Effects of surfactant treatment on mechanical and electrical properties of CNT/epoxy nanocomposites”, Composites Part A, V. 39, No. 12 (2008), 1876–1883.

[23] Jiang, X., Drzal, L. T., “Improving electrical conductivity and mechanical properties of high density polyethylene through incorporation of paraffin wax coated exfoliated grapheme nanoplatelets and multi-wall carbon nano-tubes”, Composites: Part A, V. 42 (2011), 1840–1849.

[24] Rashad, A. M. (2013). “A synopsis about the effect of nano-Al2O3, nano-Fe2O3, nano-Fe3O4 and nano- clay on some properties of cementitious materials – A short guide for Civil Engineer.” Mater. & Design, 52, 143–157.

[25] Dorigato, A., and Pegoretti, A. (2011). “The role of alumina nanoparticles in epoxy adhesives.” J. of Nanoparticle Res. 13(6), 2429–2441.

[26] Zabihi, O., Omrani, A., and Rostami, A. A. (2012). “Thermo-oxidative degradation kinetics and mechanism of the system epoxy nanocomposite reinforced with nano-Al2O3.” J. of Thermal Anal. and Calorimetry, 108(3), 1251–1260

[27] Tawfik, M.E., and Eskander, S.B. (2006) Polymer Concrete from Marble Wastes and Recycled Poly (Ethylene Terephthalate). Journal of Elastomers and Plastics 38: 65-79.

[28] Jo, B.-W., Tae, G.-H., Kim, C.-H. (2007) Uniaxial creep behavior and prediction of recycled-PET polymer concrete. Construction and Building Materials 21: 1552-1559.

[29] Bignozzi, M.C., Saccani, A., and Sandrolini, F. (2000) New Polymer Mortars Containing Polymeric Wastes. Part 1: Microstructure and Mechanical Properties. Composites, Part A: Applied Science and Manufacturing 31: 97-106.

[30] Rebeiz, K.S., Serhal, S.P., and Craft, A.P. (2004) Properties of Polymer Concrete Using Fly Ash. ASCE J. of Materials in Civil Engineering 16: 15-19.

[31] Jo, B. W., Park, S. K., Kim, D. K. (2008) Mechanical properties of nano-MMT reinforced polymer composite and polymer concrete. Construction and Building Materials 22: 14-20.

[32] Shokrieh, M. M., Kefayati, A. R., Chitsazzadeh, M. (2012) Fabrication and mechanical properties of clay/epoxy nanocomposite and its polymer concrete. Materials and Design 40: 443–452.

[33] Soliman, E., Kandil, U. F., Reda Taha, M.M. (2012) "The Significance of Carbon Nanotubes on Styrene Butadiene Rubber (SBR) and SBR Modified Mortar", Materials and Structures, 45 (6) : 803–816.

[34] Theodore, M., Hosur, M., Thomas, J., & Jeelani, S. (2011). Influence of functionalization on properties of MWCNT–epoxy nanocomposites. Materials Science & Engineering: A, 528(3).

[35] Balakrishnan, A., & Saha, M. C. (2011). Tensile fracture and thermal conductivity characterization of toughened epoxy/CNT nanocomposites. Materials Science & Engineering A, 528(3), 906-913. doi:10.1016/j.msea.2010.09.064

[36] Hameed, A., Islam, M., ahmad, I., Mahmood, N., Saeed, S., & Javed, H. (2015). Thermal and mechanical properties of carbon nanotube/epoxy nanocomposites reinforced with pristine and functionalized multiwalled carbon nanotubes. Polymer Composites, 36(10), 1891-1898. doi:10.1002/pc.23097.

[37] Patankar S.N., Mohan R., Kelkar A.D., & Vaidyanathan R. (2011). Processing and characterization of epoxy resin dispersed with multi walled carbon nanotube (MWNT) derived from camphor. Materials Science And Engineering A, 529(1), 253-256. doi:10.1016/j.msea.2011.09.025

[38] Yeh, M.-K., Hsieh, T.-H., & Tai, N.-H. (2008). Fabrication and mechanical properties of multi-walled carbon nanotubes/epoxy nanocomposites. Materials Science & Engineering A, 483-484, 289-292. doi:10.1016/j.msea.2006.09.138.

[39] Lu-Qi L., Wagner, H. D. (2007). A comparison of the mechanical strength and stiffness of MWNT-PMMA and MWNT-epoxy nanocomposites. Composite Interfaces, 14(4).

[40] Xiao, H., Song, G., Li, H., & Sun, L. (2015). Improved tensile properties of carbon nanotube modified epoxy and its continuous carbon fiber reinforced composites. Polymer Composites, 36(9), 1664-1668. doi:10.1002/pc.23076.

[41] Ghosh, P. K., Kumar, K., & Chaudhary, N. (2015). Influence of ultrasonic dual mixing on thermal and tensile properties of MWCNTs-epoxy composite. Composites Part B: Engineering, 77, 139-144. doi:10.1016/j.compositesb.2015.03.028.

[42] Chen, X., Wang, J., Lin, M., Zhong, W., Feng, T., Chen, X., ... Xue, F. (2008). Mechanical and thermal properties of epoxy nanocomposites reinforced with amino-functionalized multi-walled carbon nanotubes. Materials Science & Engineering A, 492(1-2), 236-242. doi:10.1016/j.msea.2008.04.044

[43] Sha, J., Li, G., Chen, X., Xia, P., Luo, R., Yang, S., ... Xie, L. (2016). Simultaneous ultrasonication-assisted internal mixing to prepare MWCNTs-filled epoxy composites with increased strength and thermal conductivity. Polymer Composites, 37(3), 870-880. doi:10.1002/pc.23245.

[44] Wang, Q., Dai, J., Li, W., Wei, Z., & Jiang, J. (2008). The effects of CNT alignment on electrical conductivity and mechanical properties of SWNT/epoxy nanocomposites. Composites Science & Technology, 68(7/8).

[45] Sumfleth, J., Prehn, K., Wichmann, M. H. G., Wedekind, S., & Schulte, K. (2010). A comparative study of the electrical and mechanical properties of epoxy nanocomposites reinforced by CVD- and arc-grown multi-wall carbon nanotubes. Composites Science And Technology, 70(1), 173-180. doi:10.1016/j.compscitech.2009.10.007

[46] Ganguli, S., Aglan, H., Dennig, P., & Irvin, G. (2006). Effect of Loading and Surface Modification of MWCNTs on the Fracture Behavior of Epoxy Nanocomposites. Journal Of Reinforced Plastics And Composites, 25(2), 175-188.

[47] Yu, N., Zhang, Z. H., & He, S. Y. (2008). Fracture toughness and fatigue life of MWCNT/epoxy composites. Materials Science & Engineering A, 494(1-2), 380-384. doi:10.1016/j.msea.2008.04.051

[48] Zhou, Y., Pervin, F., Lewis, L., & Jeelani, S. (2008). Fabrication and characterization of carbon/epoxy composites mixed with multi-walled carbon nanotubes. Materials Science & Engineering A, 475(1-2), 157-165. doi:10.1016/j.msea.2007.04.043

[49] Gómez-del Río, T., Salazar, A., Pearson, R. A., & Rodríguez, J. (2016). Fracture behaviour of epoxy nanocomposites modified with triblock copolymers and carbon nanotubes. Composites Part B, 87, 343-349. doi:10.1016/j.compositesb.2015.08.085

[50] Gojny, F. H., Wichmann, M. H. G., Köpke, U., Fiedler, B., & Schulte, K. (2004). Carbon nanotube-reinforced epoxy-composites: enhanced stiffness and fracture toughness at low nanotube content. Composites Science And Technology, 64(15), 2363-2371. doi:10.1016/j.compscitech.2004.04.002

[51] Park, S.-J., Heo, G.-Y., & Jin, F.-L. (2015). Rheological properties and fracture toughness of epoxy resin/multi-walled carbon nanotube composites. Polymer Engineering & Science, 55(11), 2676-2682. doi:10.1002/pen.24165

[52] White, K. L., & Sue, H. -J. (2011). Electrical conductivity and fracture behavior of epoxy/polyamide-12/multiwalled carbon nanotube composites. Polymer Engineering & Science, 51(11), 2245-2253. doi:10.1002/pen.21996

[53] Hsieh, T. H., Kinloch, A. J., Taylor, A. C., & Kinloch, I. A. (2011). The effect of carbon nanotubes on the fracture toughness and fatigue performance of a thermosetting epoxy polymer. Journal Of Materials Science: Full Set - Includes `Journal Of Materials Science Letters', 46(23), 7525-7535. doi:10.1007/s10853-011-5724-0

[54] Tang, L.-C., Wan, Y.-J., Peng, K., Pei, Y.-B., Wu, L.-B., Chen, L.-M., ... Lai, G.-Q. (2013). Fracture toughness and electrical conductivity of epoxy composites filled with

carbon nanotubes and spherical particles. Composites Part A: Applied Science And Manufacturing, 45(5453), 95-101. doi:10.1016/j.compositesa.2012.09.012

[55] Zhang, Z., Tan, Y., Wang, X., Tan, H., & Li, J. (2015). Mechanical behavior and fracture toughness of epoxy composites reinforced with combination of fibrous and spherical nanofillers. Polymer Composites, 36(12), 2147-2156. doi:10.1002/pc.23125

[56] Opelt, C. V., Becker, D., Lepienski, C. M., & Coelho, L. A. F. (2015). Reinforcement and toughening mechanisms in polymer nanocomposites – Carbon nanotubes and aluminum oxide. Composites: Part B, Engineering, 75.

[57] Seyhan, A. T., Tanoğlu, M., & Schulte, K. (2009). Tensile mechanical behavior and fracture toughness of MWCNT and DWCNT modified vinyl-ester/polyester hybrid nanocomposites produced by 3-roll milling. Materials Science & Engineering: A, 523(1/2).

[58] Ma, C., Liu, H.-Y., Du, X., Mach, L., Xu, F., & Mai, Y.-W. (2015). Fracture resistance, thermal and electrical properties of epoxy composites containing aligned carbon nanotubes by low magnetic field. Composites Science And Technology, 114, 126-135. doi:10.1016/j.compscitech.2015.04.007

[59] Ma, P. C., Kim, J.-K., & Tang, B. Z. (2007). Effects of silane functionalization on the properties of carbon nanotube/epoxy nanocomposites. Composites Science And Technology, 67(14), 2965-2972. doi:10.1016/j.compscitech.2007.05.006

[60] Balakrishnan, A., & Saha, M. C. (2011). Tensile fracture and thermal conductivity characterization of toughened epoxy/CNT nanocomposites. Materials Science & Engineering A, 528(3), 906-913. doi:10.1016/j.msea.2010.09.064

[61] AASHTO T321- 07 Determining the Fatigue Life of Compacted Hot-Mix Asphalt (HMA) Subjected to Repeated Flexural Bending (2007).

[62] ACI Committee 446, Report 5, “Fracture Toughness Testing of Concrete”, American Concrete Institute (2009).

[63] Guinea, G. V, Planas, J. and Elices, M., “A General Bilinear Fitting for the Softening Curve of Concrete”, Materials and Structures, V. 27, (1994), 99–105.

[64] Chapman. S. Clarification of the Notched Beam Level II Testing Procedures of ACI446 Committee Report 5. MS Thesis, University of New Mexico. December 2011.

[65] Reda Taha, M. M., Xiao, X., Yi, J., & Shrive, N. G. (2002). Evaluation of flexural fracture toughness for quasi-brittle structural materials using a simple test method. Canadian Journal of Civil Engineering, 29(4), 567-575. doi:10.1139/l02-044

[66] Shah, S.P., Swartz, S.E., and Ouyang, C. 1995. Fracture mechanics of concrete: applications of fracture mechanics to concrete, rock and other quasi-brittle materials. John Wiley & Sons, Inc., New York, N.Y.

[67] Meo M. and Thieulot. E. Delamination modeling in a double cantilever beam. Composite Structures 71 (2005); 429-434.

[68] Khokhar, Z. R. Ashcroft, I. A. and Silberschmidt. V. S. Interaction of matrix cracking and delamination in cross-ply laminates: Simulations with stochastic cohesive zone elements. Applied Composite Materials 18.1 (2011);3-16.

[69] ABAQUS 6.14 theory manual, ABAQUS online documentation.

[70] Abdel Wahab, M. The Mechanics of Adhesives in Composite and Metal Joints: Finite Element Analysis with ANSYS, DEStech Publications Inc., Lancaster, PA, USA, 2014

[71] Griffiths, P. de Hasseth, J.A. Fourier Transform Infrared Spectrometry, 2nd ed.; Wiley-Blackwell: Hoboken, NJ, USA, 2007.

[72] Zou, W.; Du, Z.; Liu, Y.; Yang, X.; Li, H.; Zhang, C., (2008), Functionalization of MWNTs using polyacryloyl chloride and the properties of CNT-epoxy matrix nanocomposite. Composite Science & Technology, 68 (15-16), 3259–3264.

[73] Kim, W.; Kang, S.; Ah, C.; Lee, Y.; Ha, D.; Choi, I.; Yun, W. (2004), Functionalization of shortened SWCNTs using esterification. Bull. Korean Chem. Soc., 25 (9), 1301–1302.

[74] Mikhaylova, Y., Adam, G., Häussler, L., Eichhorn, K. J., and Voit, B. (2006). “Temperature-dependent FTIR spectroscopic and thermoanalytic studies of hydrogen bonding of hydroxyl (phenolic group) terminated hyperbranched aromatic polyesters.” J. of Molecular Struct., 788(1–3), 80–88.